Article

The global hydrogen budget

https://doi.org/10.1038/s41586-025-09806-1

Received: 19 May 2024

Accepted: 24 October 2025

Published online: 17 December 2025

Open access

Check for updates

Zutao Ouyang[1,2], Robert B. Jackson[1,3,4] ✉, Marielle Saunois[5], Josep G. Canadell[6], Yuanhong Zhao[7], Catherine Morfopoulos[8], Paul B. Krummel[9], Prabir K. Patra[10], Glen P. Peters[11], Fraser Dennison[9], Thomas Gasser[5,12], Alexander T. Archibald[13], Vivek Arora[14], Gabriel Baudoin[12,15], Naveen Chandra[10], Philippe Ciais[5], Steven J. Davis[1], Sarah Feron[16], Fangzhou Guo[17], Didier Hauglustaine[5], Christopher D. Jones[18], Matthew W. Jones[19], Etsushi Kato[20], Daniel Kennedy[21], Jürgen Knauer[22,23], Sebastian Lienert[24], Danica Lombardozzi[21], Joe R. Melton[14], Julia E.M.S. Nabel[25], Michael O'Sullivan[26], Gabrielle Pétron[27], Benjamin Poulter[28], Joeri Rogelj[12,29], David Sandoval Calle[8], Pete Smith[30], Parvadha Suntharalingam[31], Hanqin Tian[32,33], Chenghao Wang[34,35] & Andy Wiltshire[18,26]

Hydrogen (H_2) will play a part in decarbonizing the global energy system[1]. However, hydrogen interacts with methane, ozone, and stratospheric water vapour, leading to an indirect 100-year global warming potential of 11 ± 4 (refs. 2–5). This raises concerns about the climate consequences of increasing H_2 use under future hydrogen economies[3,5]. A comprehensive accounting of H_2 sources and sinks is essential for assessing changes and mitigating environmental risks. Here we analyse trends in global H_2 sources and sinks from 1990 to 2020 and construct a comprehensive budget for the decade 2010–2020. H_2 sources increased from 1990 to 2020, primarily because of the oxidation of methane and anthropogenic non-methane volatile organic compounds, biogenic nitrogen fixation, and leakage from H_2 production. Sinks also increased in response to rising atmospheric H_2. Estimated global H_2 sources and sinks averaged 69.9 ± 9.4 Tg yr^{-1} and 68.4 ± 18.1 Tg yr^{-1}, respectively, for 2010–2020. Regionally, Africa and South America contained the largest sources and sinks of H_2, whereas East Asia and North America contributed the most H_2 emissions from fossil fuel combustion. We estimate that rising atmospheric H_2 between 2010 and 2020 contributed to an increase in global surface air temperature (GSAT) of 0.02 ± 0.006 °C. GSAT impacts of changing atmospheric H_2 in future marker Shared Socioeconomic Pathway scenarios are estimated to remain within 0.01–0.05 °C, depending on H_2 usage, leakage rates and CH_4 emissions that influence photochemical H_2 production.

Hydrogen (H_2) has received increased attention as an energy carrier to help decarbonize heavy industry and transport and to provide long-duration energy storage[1]. When produced by electrolysis with renewable energy, hydrogen can, in principle, be produced and consumed with near-zero carbon emissions. As a result, many energy-system scenarios project substantial growth in H_2 production and utilization this century[1,6].

At present, hydrogen production is energy- and greenhouse gas-intensive. More than 90% of hydrogen produced today is grey hydrogen, derived mainly from steam methane reforming or coal gasification, which are both carbon-intensive[1]. In anticipated net-zero scenarios, however, a shift towards cleaner, low-carbon hydrogen production is projected[1,7]. This transition encompasses both green hydrogen produced through electrolysis powered by low- or zero-carbon electricity,

[1]Department of Earth System Science, Stanford University, Stanford, CA, USA. [2]College of Forestry, Wildlife and Environment, Auburn University, Auburn, AL, USA. [3]Woods Institute for the Environment, Stanford University, Stanford, CA, USA. [4]Precourt Institute for Energy, Stanford University, Stanford, CA, USA. [5]Laboratoire des Sciences du Climat et de l'Environnement, LSCE-IPSL (CEA-CNRS-UVSQ), Université Paris-Saclay, Gif-sur-Yvette, France. [6]Global Carbon Project, CSIRO Environment, Canberra, Australian Capital Territory, Australia. [7]College of Oceanic and Atmospheric Sciences, Ocean University of China, Qingdao, China. [8]Department of Life Sciences, Imperial College London, Ascot, UK. [9]Climate, Atmosphere and Oceans Interactions, CSIRO Environment, Aspendale, Victoria, Australia. [10]Research Institute for Global Change, JAMSTEC, Yokohama, Japan. [11]CICERO Center for International Climate Research, Oslo, Norway. [12]International Institute for Applied Systems Analysis (IIASA), Laxenburg, Austria. [13]National Centre for Atmospheric Science, Yusuf Hamied Department of Chemistry, University of Cambridge, Cambridge, UK. [14]Climate Research Division, Environment and Climate Change Canada, Victoria, British Columbia, Canada. [15]Ecole Polytechnique, Palaiseau, France. [16]Knowledge Infrastructures, Campus Fryslân, University of Groningen, Groningen, The Netherlands. [17]Center for Atmospheric and Environmental Chemistry, Aerodyne Research, Billerica, MA, USA. [18]Earth System and Mitigation Science Team, Met Office Hadley Centre, Exeter, UK. [19]Tyndall Centre for Climate Change Research, School of Environmental Sciences, University of East Anglia, Norwich, UK. [20]Institute of Applied Energy (IAE), Tokyo, Japan. [21]Climate and Global Dynamics Laboratory, National Center for Atmospheric Research, Boulder, CO, USA. [22]Hawkesbury Institute for the Environment, Western Sydney University, Penrith, New South Wales, Australia. [23]School of Life Sciences, Faculty of Science, University of Technology Sydney, Ultimo, New South Wales, Australia. [24]Climate and Environmental Physics, Physics Institute and Oeschger Centre for Climate Change Research, University of Bern, Bern, Switzerland. [25]Max Planck Institute for Biogeochemistry, Jena, Germany. [26]Faculty of Environment, Science and Economy, University of Exeter, Exeter, UK. [27]Cooperative Institute for Research in Environmental Sciences, University of Colorado Boulder and NOAA Global Monitoring Laboratory, Boulder, CO, USA. [28]Spark Climate Solutions, San Francisco, CA, USA. [29]Grantham Institute - Climate Change and Environment, and Centre for Environmental Policy, Imperial College London, London, UK. [30]Institute of Biological and Environmental Sciences, University of Aberdeen, Aberdeen, UK. [31]School of Environmental Sciences, University of East Anglia, Norwich, UK. [32]Center for Earth System Science and Global Sustainability, Boston College, Schiller Institute for Integrated Science and Society, Chestnut Hill, MA, USA. [33]Department of Earth and Environmental Sciences, Boston College, Chestnut Hill, MA, USA. [34]School of Meteorology, University of Oklahoma, Norman, OK, USA. [35]Department of Geography and Environmental Sustainability, University of Oklahoma, Norman, OK, USA. ✉e-mail: rob.jackson@stanford.edu

and blue hydrogen generated by reforming fossil fuels coupled with carbon capture and storage. Ultimately, green and blue hydrogen are projected to dominate hydrogen manufacturing by 2030–2040 (ref. 6).

Excessive atmospheric H_2 has climate consequences. Despite its relatively short lifetime of 1.9–2.7 years (ref. 5), H_2 acts as an indirect greenhouse gas. By consuming OH radicals, a crucial sink for CH_4, H_2 warms the climate indirectly by extending the lifetime of CH_4, producing greenhouse gases such as ozone and stratospheric water vapour, and affecting the formation of aerosols and clouds[2,5]. Recent studies estimate 20-year and 100-year global warming potentials for H_2 of 37 ± 18 and 11 ± 4, respectively[2–5] (Supplementary Table 1). Understanding the impact of hydrogen leakage is, therefore, necessary to realize the full climate benefits of the H_2 economy[2,3,8–10]. For blue hydrogen, additional climate impacts arise from fugitive CH_4 emissions and uncaptured CO_2, which, in scenarios with relatively high H_2 and CH_4 emissions, can result in greater warming than directly burning natural gas[3,11].

H_2 concentrations in the atmosphere increased by about 70% from preindustrial times through 2003, after which time its concentration briefly stabilized[12,13]. However, H_2 concentrations began increasing again around 2010 (ref. 14) (Supplementary Note 1), reaching an annual mean level of around 555 ppb in 2024 (ref. 15). The reasons for this recent rise remain poorly quantified.

Here, we examine the trends of H_2 sources and sinks over the past three decades (1990–2020) and construct a comprehensive global budget for the most recent decade (2010–2020) with gridded sources and sinks (Extended Data Fig. 1). We use bottom-up approaches for estimating H_2 sources and sinks. These approaches combine activity data, H_2 emission factors, and emission factors or emission inventories of precursor species with process-based modelling. Using an ensemble of synthesized activity data, updated emission inventories, recently published emission factors and new observational measurements, we also provide detailed uncertainty estimates for key H_2 sources and sinks, which were poorly characterized previously.

With this comprehensive budget as a baseline for assessing future changes, we further estimate the climate impact of increasing H_2 concentrations historically and in future global H_2 economies.

Three decades (1990–2020) of global H_2 sources and sinks

The earliest global H_2 budget traces back to the 1980s (ref. 16), with several later updates[17–23]. None of these previous studies fully examined recent changes in the H_2 budget attributable to rapid changes in the emissions and processes of precursor gases, particularly CH_4 and non-methane volatile organic compounds (NMVOCs), or for OH burdens, H_2 concentrations and terrestrial and technological processes.

We estimate that increasing H_2 emissions from 1990 to 2020 arose predominantly from anthropogenic sources (that is, oxidation of increased levels of CH_4 and anthropogenic NMVOCs and leakage from H_2 production) (Fig. 1). By contrast, natural sources such as fire emissions and biogenic NMVOC oxidation show substantial interannual variation but no notable trends over this period (Fig. 1). The global surface average H_2 concentration increased from 523.4 ppb in 1992 to 543.5 ppb in 2020, a 3.8% increase, consistent with the increasing anthropogenic emissions of CH_4 and NMVOCs during the study period.

We estimate H_2 production from CH_4 oxidation to be the largest increasing source from 1990 to 2020 (0.1 Tg yr^{-1} or a total increase of about 4 Tg), attributable mainly to increasing atmospheric CH_4 from anthropogenic activities[24], but there was also a sudden decrease in 2020 attributable to COVID-19 (Fig. 1). H_2 leakage from H_2 production increased at an estimated rate of 0.015 Tg yr^{-1} because of an increasing industrial usage of H_2 (that is, a total increase of around 0.45 Tg from 1990 to 2020) (Fig. 1). H_2 emissions from the oxidation of anthropogenic NMVOCs and biogenic nitrogen fixation (BNF) increased at an estimated rate of 0.005 Tg yr^{-1} and 0.008 Tg yr^{-1}, respectively (Fig. 1). H_2 is produced naturally from BNF, but the increase is probably attributable to increased anthropogenic cultivation of leguminous crops[25]. Some anthropogenic sources of H_2 seem to be decreasing, such as direct emissions from the combustion of fossil fuels and biofuels (estimated declines of −0.1 Tg H_2 yr^{-1} and −0.03 Tg H_2 yr^{-1}, respectively), most likely attributable to improvements in combustion efficiency in engines that reduce incomplete combustion[26]. Nevertheless, we acknowledge that the H_2/CO emission ratio may have evolved over time as technology improves, but a constant H_2/CO ratio was assumed in this study.

Both the global soil and OH sinks increased significantly over the 1992–2020 period at rates of 0.05 Tg yr^{-1} and 0.06 Tg yr^{-1} ($P \ll 0.01$), respectively, attributable to increasing H_2 in the atmosphere (Fig. 1). We also estimate a small but significant increase in the global average soil H_2 deposit velocity (slope = 7×10^{-6} cm s^{-1} yr^{-1}, $P < 0.05$) in 1992–2020.

The global H_2 budget (2010–2020)

We estimate the global H_2 budget for the recent decade (2010–2020) by synthesizing multiple datasets and models, incorporating uncertainties propagated from multiple levels, including activity data, precursor emissions, and emission factors for both precursor species and H_2 (Methods). No previous analysis, to our knowledge, estimated the uncertainties of these sink/source terms by synthesizing multiple datasets or modelling analyses as done here.

We estimate mean global H_2 sources and sinks to be 69.9 ± 9.4 Tg yr^{-1} and 68.4 ± 18.1 Tg yr^{-1}, respectively, for the decade 2010–2020 (Fig. 2). The largest anthropogenic sources of H_2 over this decade include those from fossil fuel and biofuel combustion, leakage from industrial H_2 production, and oxidation of CH_4 and anthropogenic NMVOCs (Fig. 2). Photochemical oxidation is the largest H_2 source (an estimated 38.4 Tg yr^{-1}, 56% of the global total), whereas soil uptake is the largest sink (an estimated 50.0 Tg yr^{-1}, 73% of total sinks) (Fig. 2). Soil uptake contributes the largest uncertainty to our total budget uncertainty, followed by photochemical oxidation, fossil fuel combustion, BNF, and biomass and biofuel burning.

The H_2 budget was further evaluated using a two-box model (Supplementary Note 2) to optimize total sources or total sinks for 2010–2020. Our bottom-up imbalance based on mean total sinks and sources is 1.5 ± 20.4 Tg yr^{-1}, whereas the optimized imbalance is 0.6 ± 1.4 Tg yr^{-1} at a mean atmospheric lifetime for H_2 of 2.8 years (Extended Data Table 1). The mean difference between previous and optimized values is less than 1 Tg yr^{-1}, within the uncertainty range of the priors, indicating that only a modest adjustment to either emissions or losses can considerably improve agreement with observed atmospheric H_2. Our estimated balance between emissions and losses also closely matches the interannual burden change ($R^2 = 0.42$).

Our global total source estimate falls within the range of previous estimates for earlier time periods (Supplementary Table 2). However, it is approximately 30 Tg smaller than the two previous atmospheric inversion studies[18,20], which probably overestimated H_2 production from NMVOCs (>36 Tg yr^{-1}) for the following reasons. These higher estimates conflict with the well-established NMVOC production levels of carbon monoxide (CO), whose primary removal mechanism (reaction with OH, about 90%) is widely recognized to limit its sources. Moreover, satellite observation of atmospheric formaldehyde (HCHO), which is produced from NMVOCs to generate H_2, does not support such a high level of NMVOC production of H_2 (Methods).

Our estimate of total sinks agrees well with most previous studies[17,21,22,27–30]. We estimated OH oxidation and its uncertainties based on an ensemble of eight OH datasets and the soil sink and its uncertainty based on seven different model parameterization and 10 different soil attribution inputs (Methods).

The spatial distribution of sources is more uneven than for sinks (Fig. 3). Hotspots of H_2 emissions are evident, with the highest density of emissions observed in Southeast and East Asia. However, tropical

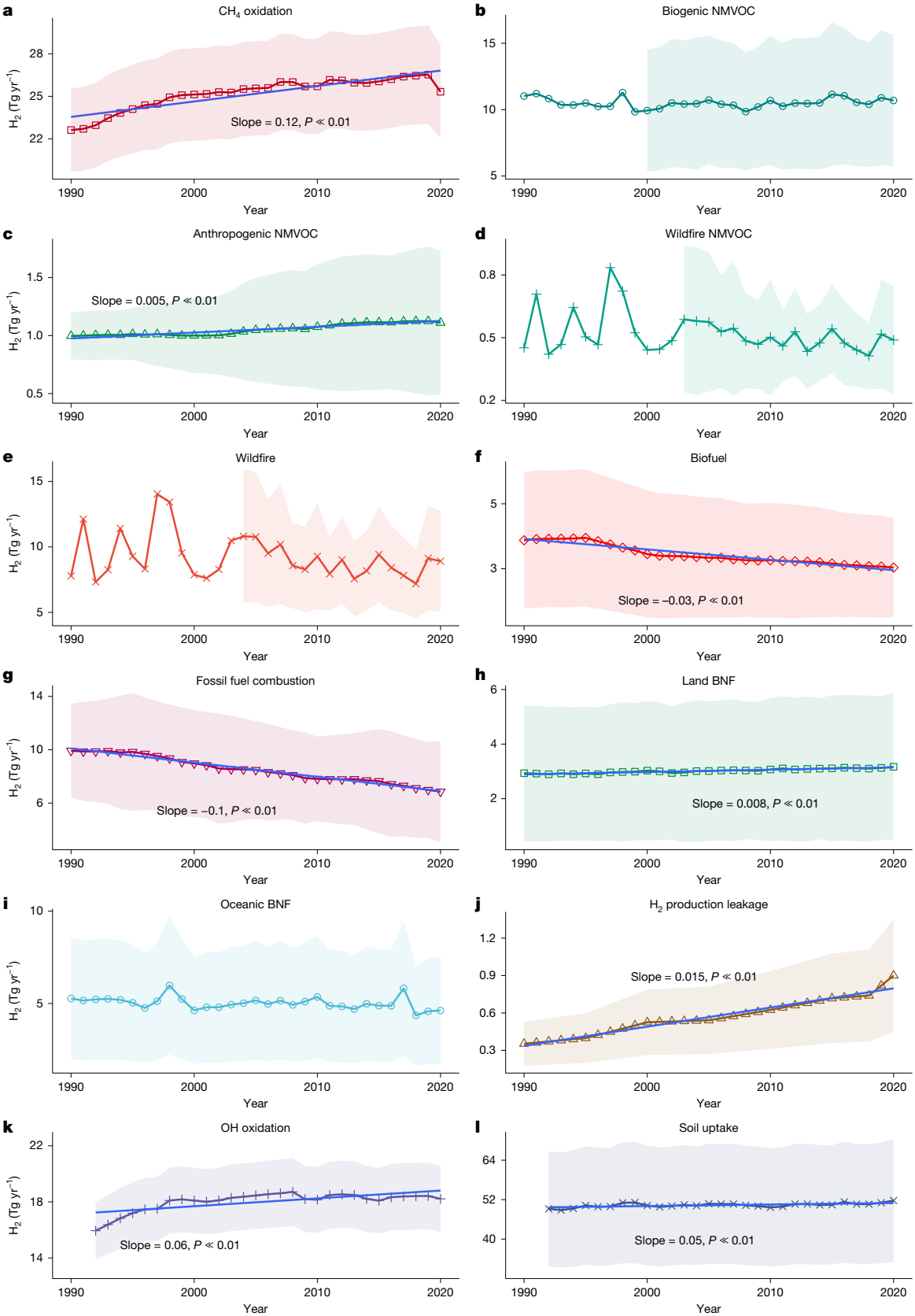

Fig. 1 | Global sources and sinks of H_2 (Tg H_2 yr^{-1}) over three decades (1990–2020). a–**j**, The H_2 sources include production from oxidation of CH_4 (**a**), biogenic NMVOCs (**b**), anthropogenic NMVOCs (**c**) and wildfire NMVOCs (**d**); as well as direct H_2 emissions from wildfires (**e**), combustion of biofuels (**f**), the combustion of fossil fuels (**g**), biological nitrogen fixation on land (**h**) or in the oceans (**i**), and H_2 leakage during industrial H_2 production (**j**). **k**,**l**, The sinks (bottom two panels) include H_2 oxidized by OH (**k**) and H_2 uptake by microbes in soils (**l**). The category 'Anthropogenic NMVOC' (**c**) includes emissions of NMVOCs from burning both fossil fuels and biofuels. Note that some minor sources shown in Fig. 2 are omitted for this time series analysis. Uncertainties (shaded regions) represent standard deviations (1 s.d. above and below the line).

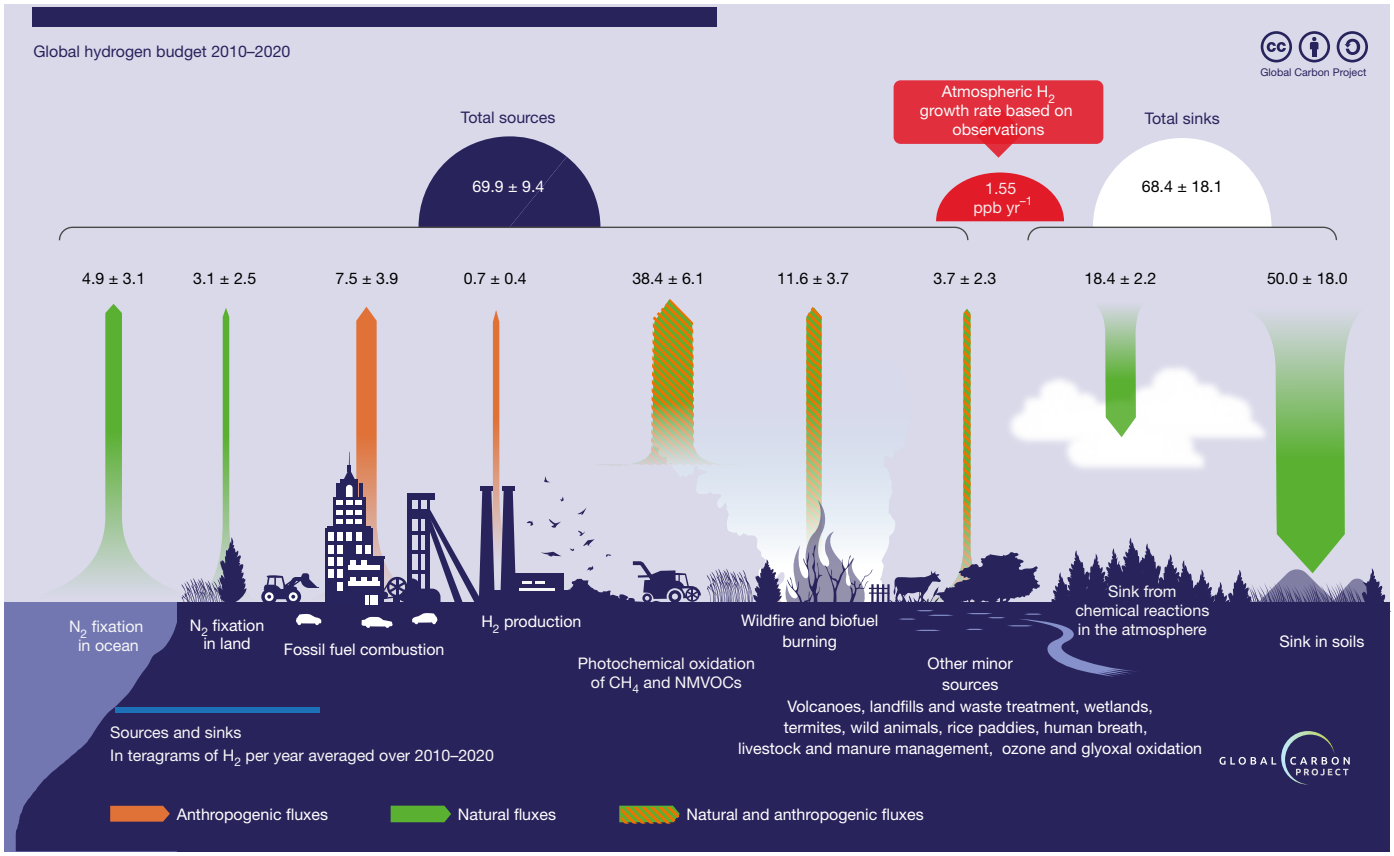

Fig. 2 | The main sources and sinks of H_2. The main sources (upward arrows) and sinks (downward arrows) of H_2 (Tg yr^{-1}) for anthropogenic (orange), natural (green) and mixed anthropogenic and natural fluxes (hatched). Dominant sources include photochemical oxidation of both CH_4 and non-methane volatile organic compounds (NMVOCs), combustion of biomass and fossil fuels and H_2 production from nitrogen fixation. The dominant global sinks of H_2 are consumption by soil microbes and oxidation by tropospheric hydroxyl radicals (OH).

regions contribute the largest share (about 60%) of the total amount of emissions and production (Fig. 3a). This result is attributable to the combination of higher temperatures in the tropics promoting CH_4 and NMVOC oxidation, abundant plant biomass that leads to relatively high biogenic NMVOC emissions, and frequent tropical fires. Although the distribution of H_2 sinks is more uniform across non-desert and non-frozen lands globally, tropical regions still account for the largest sink (around 50% of the global total) (Fig. 3b).

Photochemical H_2 production

H_2 is produced in the atmosphere through the photolysis of formaldehyde (HCHO) (ref. 17). HCHO is produced by the oxidation of CH_4 and NMVOCs by OH, with yields affected by levels of NO_x gases[31]. Previous estimates of production from CH_4 oxidation range from 15 Tg yr^{-1} to 27 Tg yr^{-1} (refs. 21,23,28), but earlier studies either did not report uncertainties or disclosed much larger uncertainties (≥±8 Tg yr^{-1}) (refs. 17,21) than ours (± 3.5 Tg yr^{-1}). We estimate a relatively higher average rate of 26.1 ± 3.5 Tg H_2 yr^{-1} for this source (Supplementary Table 2), primarily attributable to increasing atmospheric CH_4.

Various NMVOCs, including biogenic sources, anthropogenic sources and mixed sources such as biomass burning, produce atmospheric H_2 through photochemical oxidation. We estimate that biogenic, wildfire and anthropogenic NMVOCs contribute 10.7 ± 5.0 Tg yr^{-1}, 0.5 ± 0.3 Tg yr^{-1} and 1.1 ± 0.6 Tg yr^{-1}, respectively (Extended Data Table 1), summing to 12.3 ± 5.0 Tg yr^{-1}.

Combining CH_4 and NMVOCs oxidation, we estimate total photochemical sources of H_2 to be 38.4 ± 6.1 Tg yr^{-1} for the decade 2010–2020. This quantity lies within the range of previous estimates (31–87 Tg yr^{-1}) and aligns well with a few estimates in other periods using three-dimensional (3D) chemical transport models[18,22,30] (Supplementary Table 2).

Direct H_2 emissions from combustion

Incomplete combustion generates CO, which can undergo the water–gas shift reaction to produce H_2 (ref. 17). Automobile transportation is the primary H_2 source from fossil fuel combustion, although other processes involving fossil fuel or biomass combustion also emit H_2.

Based on CO emissions and CO/H_2 emission ratios across various sectors of fossil fuel and biomass combustion (Methods), we estimate total H_2 emissions from fossil fuel combustion to be 7.5 ± 3.9 Tg yr^{-1} (3.7 ± 2.0 Tg yr^{-1} for automobile transport and 3.8 ± 3.3 Tg yr^{-1} from other fossil sources) and from biomass burning to be 11.6 ± 3.7 Tg yr^{-1} (8.4 ± 3.3 Tg yr^{-1} for wildfires and 3.2 ± 1.7 Tg yr^{-1} for biofuels) during 2010–2020. Our estimate of H_2 emissions from fossil fuel combustion is lower than that in previous studies (Supplementary Table 2). Our estimate of H_2 emissions from biomass burning (11.6 ± 3.7 Tg yr^{-1}) falls within the range of previous estimates[17,18,21,28–30,32].

Leakage from H_2 production

Similar to methane leakage from the natural gas industry, the production, distribution and utilization of H_2 have some unavoidable leakage. At present, however, the vast majority of H_2 production (>99%) is consumed locally at the site of production for industrial processes[1]. Estimates of current H_2 leakage, therefore, mainly consider leakage at production sites. The average global leakage rate for H_2 production is

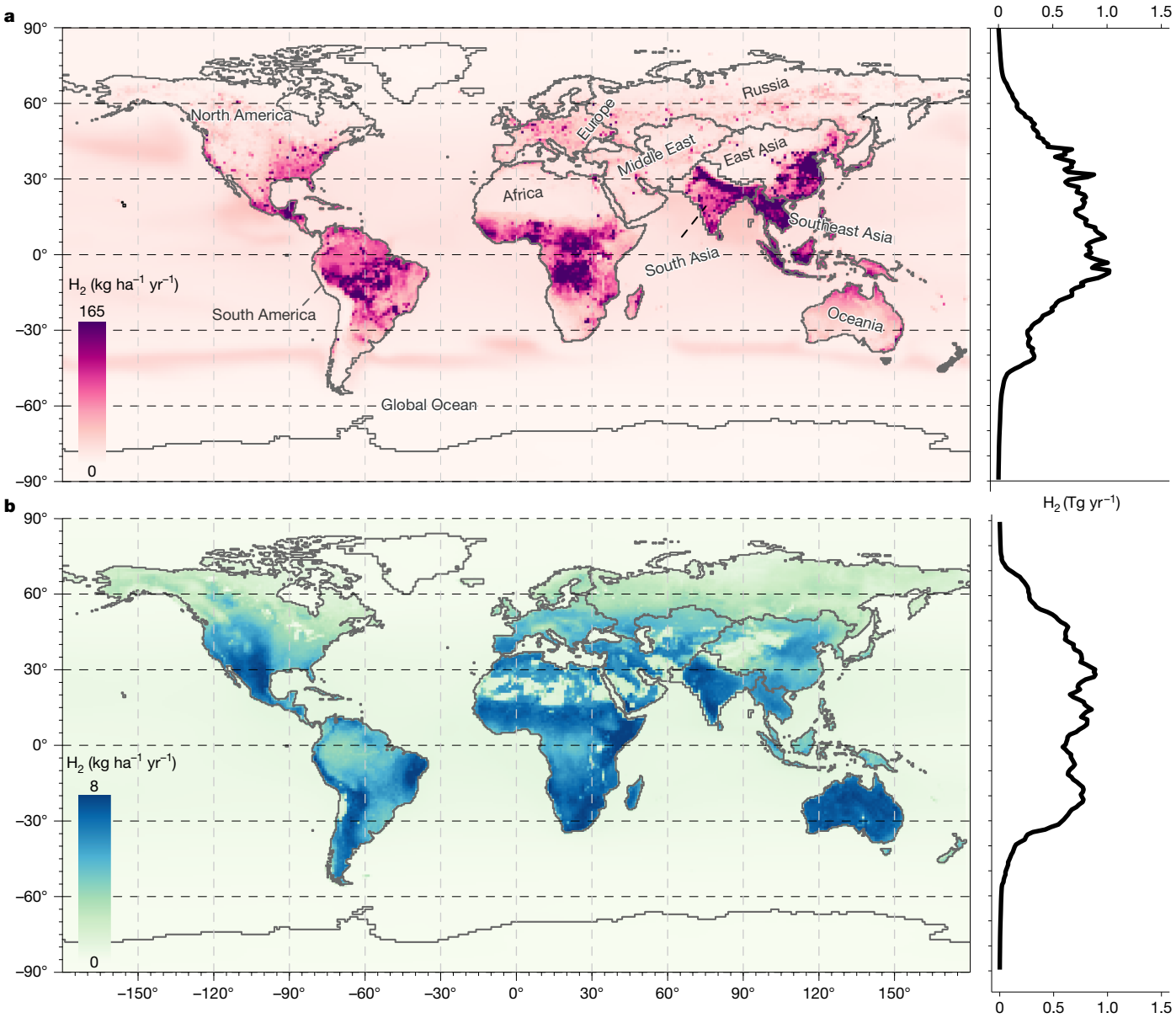

Fig. 3 | The spatial distribution of total sources and sinks of hydrogen. **a**, Total sources gridded spatially (top left) and the latitudinal distribution of sources (top right). **b**, Total sinks gridded spatially (bottom left) and latitudinally (bottom right). The 10 land regions of Earth follow the categorizations in the second phase of the REgional Carbon Cycle Assessment and Processes Project (RECCAP-2)[59] and are labelled in **a**. These regions are used subsequently to analyse regional sources and sinks. The total sources here include only the photochemical oxidation of CH_4 and NMVOCs, direct emissions from fires and the combustion of fossil fuels and biofuels, and emissions from biological nitrogen fixation terrestrially and in the oceans.

relatively unconstrained because of a lack of measurements. Using a 1 ± 0.5% leakage rate for industrial H_2 production (Methods), we estimate total H_2 leakage at 0.7 ± 0.4 Tg yr^{-1} for 2010–2020 (Fig. 1), within the range of previous estimates[23,33].

H_2 emission from BNF

H_2 is produced as a by-product of BNF[34], a widespread process carried out by symbiotic and free-living bacteria. However, the H_2 sources from oceanic and terrestrial BNF remain relatively poorly constrained. Previous estimates suggest a range of 0–11 Tg yr^{-1} from land and oceans combined (Supplementary Table 2).

Some studies ignored land-based sources of H_2 from BNF, arguing that most soil H_2 production is consumed by soil hydrogenases[29]. However, observations in various land covers show H_2 escaping from the soil to the atmosphere[34,35], indicating the importance of this source. Through an ensemble of models that estimated N fixation from BNF and newly compiled H_2/N_2 net production ratios (Methods), we estimate a new land-based H_2 emission to be 3.1 ± 2.5 Tg yr^{-1} for the period 2010–2020 (Fig. 1).

Previous studies observed H_2 supersaturation in oceans with respect to atmospheric H_2 (refs. 36–39), leading to H_2 release into the atmosphere. Oceanic H_2 mainly originates from cyanobacterial BNF, although other origins are possible[17,40]. Using our newly compiled H_2/N_2 net production ratios from the literature (Methods), we estimate the total oceanic BNF H_2 emission to be 4.9 ± 3.1 Tg yr^{-1} for 2010–2020 (Fig. 1).

Other minor H_2 sources

There are additional minor H_2 sources (usually <1.0 Tg H_2 yr^{-1}) with substantial uncertainties. Our budget accounts for one geological source (volcanic emissions) and eight fermentation processes

(the breakdown of organic materials under anaerobic conditions) occurring in wetlands, rice paddies, landfills, waste treatment, livestock production (that is, enteric fermentation and manure management), termites, wild animals and human breath, along with two photochemical processes (the photolysis of ozone and glyoxal). Collectively, we estimate a total of 3.7 ± 2.3 Tg H_2 yr^{-1} from these minor sources (Fig. 2) based on sparse data of emission factors compiled from the literature (Methods). Although individually small compared with major sources, their cumulative emissions nevertheless represent a substantial contribution to atmospheric H_2 and warrant further study and elucidation.

H_2 sinks

Previous estimates of global soil H_2 uptake ranged widely from 15 Tg yr^{-1} to 99 Tg yr^{-1} (Supplementary Table 2). We used the process-based model formulation in ref. 41 to estimate global soil H_2 uptake with seven sets of parameterizations. Soil properties are recognized as a large source of uncertainty[42]. We thus also integrated forcing data for soil texture, porosity, temperature, moisture and snow depth from an ensemble of 10 global models to estimate this uncertainty. We estimate a global H_2 soil uptake rate of 50.0 ± 18.0 Tg yr^{-1} for the period 2010–2020 (Fig. 2), a range that includes most previous estimates (Supplementary Table 2).

The loss of H_2 through reactions with OH in the atmosphere is relatively well-constrained compared with soil uptake. However, it carries uncertainty attributable in part to variations in OH distributions and trends. By considering the 3D distribution of OH and H_2, along with temperature-dependent reaction rates[43], we estimate this loss of H_2 to be 18.4 ± 2.2 Tg yr^{-1} during the decade 2010–2020. Our estimate is also consistent with most previous studies[17,18,20–22,30,32,44] (Supplementary Table 2).

Regional sources and sinks (2010–2020)

Our estimates show strong regional differences in the magnitude of H_2 sources and sinks (Fig. 4). Most H_2 photochemical production/loss occurs over the oceans, because of their large global area, particularly in the tropics, in which both OH concentrations and temperatures are relatively high. On land, Europe is the smallest regional source of H_2 (<2% of global total), whereas Africa and South America stand out as the largest two regional sources (about 16% and 11% of the global total, respectively) (Supplementary Table 3). Africa is also the largest regional sink for H_2 (about 23% of the global total), followed by South America as the second largest (around 13% of global total). Southeast Asia is the smallest regional sink (approximately 4% of the global total) (Supplementary Table 3).

The two largest economic regions of the world, East Asia and North America, contribute the most H_2 emissions from fossil fuel combustion (about 32% and 15% of the global total, respectively; Supplementary Table 3). South America is the largest contributor of H_2 from land-based BNF (27% of the terrestrial total). This result can be attributed to its extensive cultivation of leguminous plants such as soybeans and peanuts[45], as well as extensive tropical areas in which native species fix nitrogen[46].

H_2 generated from biomass combustion, NMVOCs and CH_4 oxidation comprise the dominant sources in Africa and South America (Fig. 4). In Africa, biomass combustion, mostly through wildfires, constitutes the largest source, followed by NMVOC oxidation (Fig. 4). In South America, NMVOC oxidation is the largest source, followed by biomass combustion (Fig. 4). Both Africa and South America have extensive tropical areas and are characterized by frequent wildfires[47] and abundant vegetation that produces NMVOCs[48]. H_2 emissions from fossil fuel combustion comprise the largest source of H_2 in East Asia, North America and Europe (Fig. 4), consistent with more intensive fossil fuel use there.

Climate impacts of atmospheric H_2

We estimate changes in atmospheric H_2 and their associated impact on GSAT using the compact Earth system model OSCAR[49], which integrates the hydrogen cycle and its interactions with methane (CH_4) (Methods). Unlike previous studies that primarily assess the net climate benefits of H_2 by examining tradeoffs between reductions in greenhouse gas emissions and potential H_2 leakage[3,50], our work estimates changes in the H_2 budget and quantifies the missing warming in the current climate simulations due to the lack of an interactive representation of the H_2–CH_4 system in most models.

Over the past decade (2010–2020), we estimate that rising atmospheric H_2 concentrations have contributed to an increase in GSAT of 0.020 ± 0.006 °C with respect to the preindustrial period. For the future, we project all components of the H_2 budget using IPCC AR6 marker Shared Socioeconomic Pathway (SSP) climate scenarios[51] to estimate the changes in atmospheric H_2 and the resulting climate impacts not currently included in these SSP climate projections.

The future contribution of H_2 to GSAT depends on how much H_2 is consumed as an energy carrier (Fig. 5a), leaks during usage (Fig. 5b) and is produced through the photolysis of CH_4 in the atmosphere (Fig. 5e, as photolysis of NMVOCs is not projected to change much) and other H_2 emissions (Fig. 5c,d). In low-warming scenarios with high H_2 usage (for example, SSP1-1.9 and SSP1-2.6; Fig. 5a), methane emissions are substantially mitigated, which reduces the formation of H_2 from CH_4 by photolysis (Fig. 5e). Therefore, the warming from H_2 could even decrease slightly from the present-day level if H_2 leakage is relatively low (for example, 1% leakage, Fig. 5g) but still increase if leakage is high (for example, 10% leakage, Fig. 5h). In a medium-warming scenario such as SSP2-4.5, methane emissions decline only slightly, and the change in warming from H_2 is predominately determined by the H_2 leakage rate: it may be similar to today under low leakage rates but increase substantially under higher leakage (Fig. 5g,h) (acknowledging that such a high H_2 usage is specific to this SSP2-4.5 (ref. 52) of the SSPs we examined; Fig. 5a). In higher-warming scenarios (for example, SSP 4-6.0 or SSP5-8.5), the H_2 use is relatively low but methane emissions remain largely unmitigated. In these cases, the additional H_2 formed from CH_4 photolysis can outweigh the H_2 that leaks from the system under both low and high H_2 leakage scenarios (Fig. 5g,h), increasing H_2-induced GSAT. Overall, this compensation effect caused by inversely related CH_4 and H_2 emissions across these limited SSP scenarios leads to a missing warming in climate projections of 0.01–0.05 °C, which is relatively small compared with the long-term total temperature decrease in mitigation, that is, about 1.0 °C in SSP2-4.5 (current policies), about 1.9 °C in SSP1-2.6 and about 2.5 °C in SSP1-1.9 compared with an SSP3-7.0 (baseline)[51]. However, if there were scenarios with both high demand and leakage rates for H_2, as well as unmitigated CH_4 emissions, the potential warming resulting from increasing H_2 concentrations would be considerably larger than those shown in Fig. 5.

Discussion

Our new global H_2 budget for the recent decade 2010–2020 was estimated by synthesizing multiple datasets and models, with each budget term estimated individually using a bottom-up synthesis approach. When combined with atmospheric H_2 observation data[15], our gridded H_2 sources and sinks can provide data needed for further optimization of the global H_2 budget by top-down atmospheric inversions and bottom-up chemistry transport models.

Our work also highlights remaining uncertainties in sources and sinks, and research needs to constrain the global H_2 budget further. The largest uncertainty arises from the soil uptake term, which is sensitive to both model parameterization (especially the value of the maximum biological uptake rate) and intermodel variation of soil attributes. Refined quantification of soil characteristics (for example,

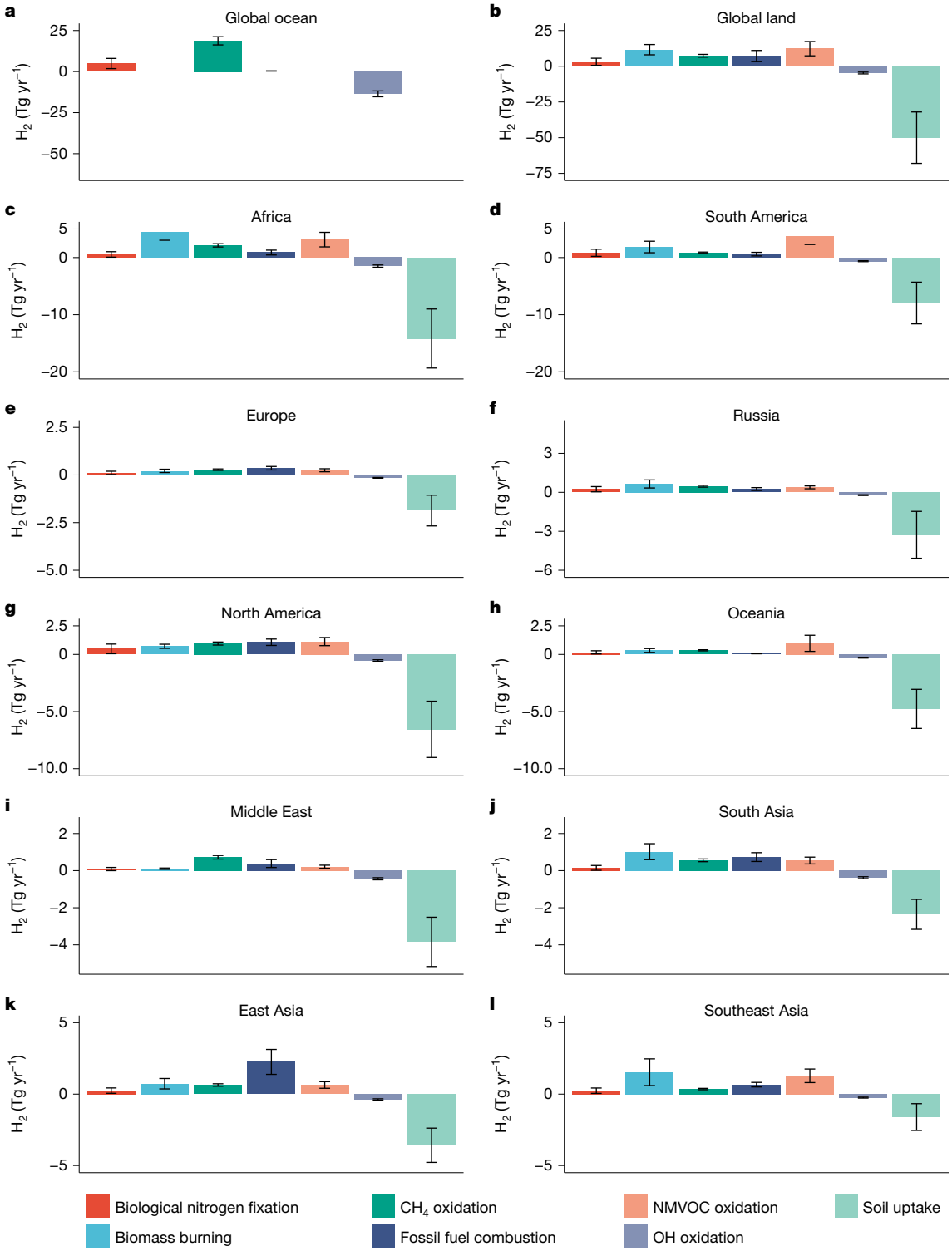

Fig. 4 | Regional sources and sinks of H_2 (Tg H_2 yr^{-1}) averaged for the decade 2010–2020. a,**b**, The Earth is partitioned into global ocean (**a**) and global land (**b**). **c**–**l**, The ice-free land of Earth is further partitioned into 10 regions following the definitions used in the second phase of the Regional Carbon Cycle Assessment and Processes Project (RECCAP-2)[59]: Africa (**c**), South America (**d**), Europe (**e**), Russia (**f**), North America (**g**), Oceania (**h**), Middle East (**i**), South Asia (**j**), East Asia (**k**) and Southeast Asia (**l**). Each subplot shows the emissions from five source terms (shown as positive values) and two sink terms (shown as negative values). Minor source terms and H_2 leakage (Fig. 2) are not shown here.

soil porosity, composition, moisture and temperature) and understanding of how they influence microbial hydrogenases are needed to improve modelling of soil H_2 uptake. More in situ measurements of soil uptake rates are needed in different ecosystems and seasons to better validate, parameterize and constrain process-based H_2 uptake models. Moreover, more laboratory studies are needed to constrain the maximum biological H_2 uptake in different soil types and microbial communities.

Uncertainties associated with other sources and sinks are smaller than for the soil sink in absolute terms but can still be larger in relative

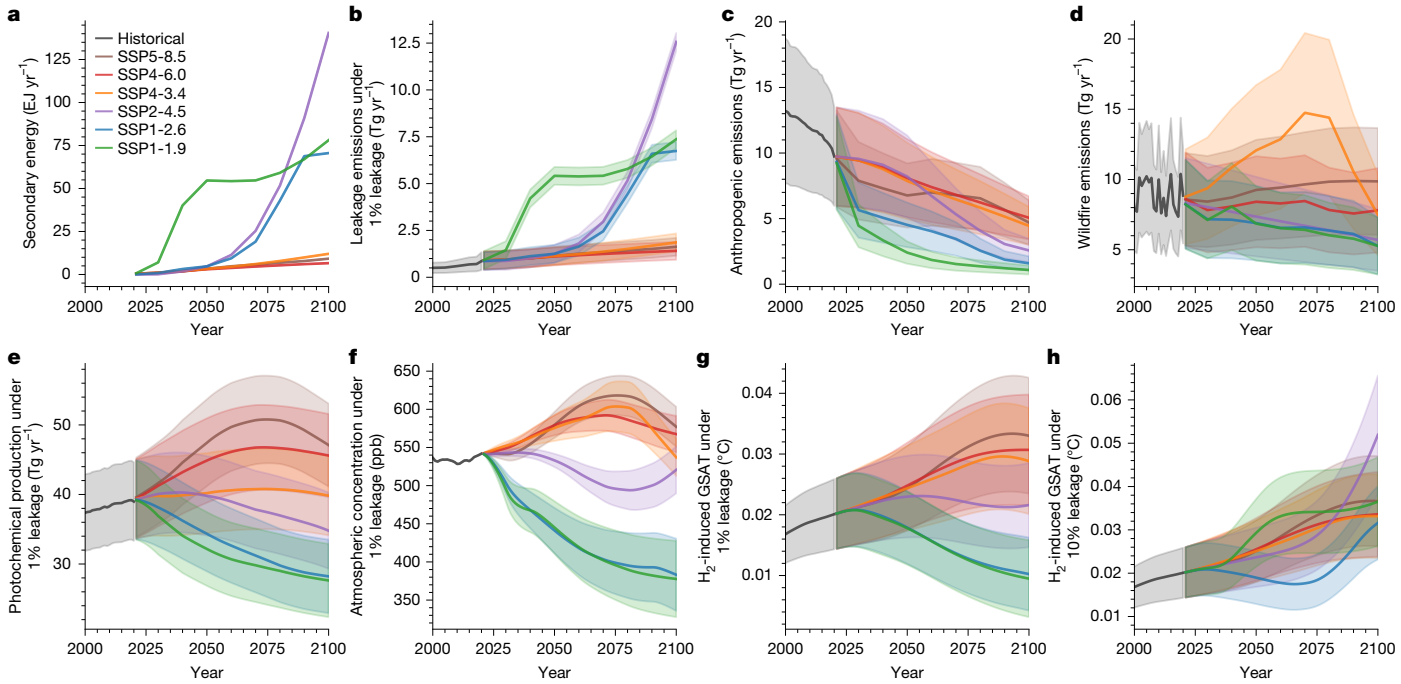

Fig. 5 | Projected global hydrogen use (EJ yr^{-1}), emissions (Tg yr^{-1}), atmospheric concentration (ppb), and climate impacts (°C) under varying leakage scenarios in marker SSP scenarios as used in IPCC AR6. a, Hydrogen as secondary energy in SSP scenarios through 2100. **b**, Corresponding leakage emissions by scenario under 1% H_2 leakage rate. **c**, Future anthropogenic emissions (fossil, biofuel and other minor sources). **d**, Future wildfire emissions. **e**, Total H_2 production from CH_4 and VOCs oxidation under 1% leakage rate. **f**, Atmospheric concentration of H_2 under 1% leakage rate. **g**,**h**, GSAT impact from H_2 concentration change under 1% (**g**) and 10% (**h**) leakage rates. The shaded regions represent 1 s.d. GSAT impact for other intermediate leakage rates (3% and 5%) can be found in Extended Data Fig. 2.

terms, and future work is needed to reduce these uncertainties. Increased H_2 production from CH_4 oxidation is probably the main reason for the increasing H_2 concentration in the atmosphere over the past decade, a conclusion that would benefit from further observations and studies to verify. The atmospheric distribution of CH_4 and the H_2-yielding mechanism of CH_4 oxidation are now fairly well understood, leading to a reduced uncertainty in H_2 source estimates from this process. However, the distribution of NMVOC and the molar yields of H_2 from NMVOC oxidation need further quantification across space and time. Other remaining uncertainties include estimates related to OH fields, particularly as the abundance of methyl chloroform declines below 1 pptv (parts per trillion by volume). Minimizing this uncertainty could further improve estimated photochemical production and loss of H_2.

There remains a substantial lack of empirical data on H_2 emission factors for various sectors, including minor sources, and more measurements are needed to improve the estimate to better constrain the global budget. More data are needed on leakage rates of H_2 in production sites, transport pipelines, and end-use facilities and appliances. Limited data also exist for H_2 emission factors for fossil fuel and biofuel combustion, nitrogen fixation processes on land and in the oceans, and for minor sources such as emissions from geological sources, wet soils (for example, wetlands, landfills and rice paddies) and enteric fermentation (for example, termites, and livestock), and photolysis of ozone and glyoxal. We summarize current data availability and gaps in Extended Data Table 2.

This lack of empirical emission data is caused largely by a lack of mobile or portable instruments that can quantify H_2 concentrations in air. For methane, for instance, laser-based instruments are available that measure CH_4 at low concentrations with relatively high precision and fast response. These instruments are used to quantify emission fluxes in chamber measurements, eddy covariance and tower monitoring, and in mobile and aerial measurements. The only commercially available H_2 instrument of comparable performance that we know of is the TILDAS H_2 Monitor manufactured by Aerodyne since 2024. This instrument was tested recently with controlled-release experiments to quantify H_2 emissions using a mobile platform[53]. However, to our knowledge, no H_2 monitors are as yet available for aerial, satellite and long-term tower-based monitoring.

Further work is needed to estimate sources and sinks that are potentially unaccounted for, including geologic seeps, pipeline leakage and vegetation. For example, we had insufficient data to consider geologic sources from geothermal seeps, hot springs and oceanic crusts beyond volcanoes. Moreover, there is limited data on H_2 leakage from natural gas systems, despite some commercial natural gas already containing blended H_2 (refs. 54,55).

Plant measurements are also needed because vegetation can be both a sink and a source of H_2. A Harvard Forest study observed unexpected aboveground emissions of H_2 during leaf senescence[56], although the mechanism of this emission was unclear. It may be a secondary emission, perhaps the oxidation of VOCs released by plants that are already accounted for in our current H_2 budget. However, if it is direct emission from plants, this could be a new source not included at present in H_2 budgets. Vegetation may also be an H_2 sink, as some research suggests that tree foliage and bark exhibit the capacity to absorb CH_4 (refs. 57,58). It is therefore possible, perhaps likely, that H_2-producing and H_2-consuming microbes coexist, as they do for CH_4.

We found that rising atmospheric H_2 between 2010 and 2020 contributed to an increase in GSAT of 0.020 ± 0.006 °C. Future climate impact could either decrease or increase depending on H_2 usage and leakage rates and CH_4 emissions but is expected to remain within 0.01–0.05 °C under IPCC marker SSP scenarios. Our results underscore the need for a deeper scientific understanding of the global hydrogen cycle and its links to radiative forcing to support a climate-safe and sustainable hydrogen economy.

Online content

Any methods, additional references, Nature Portfolio reporting summaries, source data, extended data, supplementary information, acknowledgements, peer review information; details of author contributions and competing interests; and statements of data and code availability are available at https://doi.org/10.1038/s41586-025-09806-1.

1. International Energy Agency. *Global Hydrogen Review 2023* (OECD Publishing, 2023).
2. Warwick, N. J. et al. Atmospheric composition and climate impacts of a future hydrogen economy. *Atmos. Chem. Phys.* **23**, 13451–13467 (2023).
3. Hauglustaine, D. et al. Climate benefit of a future hydrogen economy. *Commun. Earth Environ.* **3**, 295 (2022).
4. Derwent, R. G. Global warming potential (GWP) for hydrogen: sensitivities, uncertainties and meta-analysis. *Int. J. Hydrogen Energy* **48**, 2022–8341 (2022).
5. Sand, M. et al. A multi-model assessment of the Global Warming Potential of hydrogen. *Commun. Earth Environ* **4**, 203 (2023).
6. *Hydrogen Decarbonization Pathways: Potential Supply Scenarios* (Hydrogen Council, 2021).
7. IPCC. (eds Shukla, P. R. et al.) (Cambridge Univ. Press, 2022).
8. Jacobson, M. Z. Effects of wind-powered hydrogen fuel cell vehicles on stratospheric ozone and global climate. *Geophys. Res. Lett.* **35**, L19803 (2008).
9. van Ruijven, B., Lamarque, J.-F., van Vuuren, D. P., Kram, T. & Eerens, H. Emission scenarios for a global hydrogen economy and the consequences for global air pollution. *Glob. Environ. Change* **21**, 983–994 (2011).
10. Schultz, M. G., Diehl, T., Brasseur, G. P. & Zittel, W. Air pollution and climate-forcing impacts of a global hydrogen economy. *Science* **302**, 624–627 (2003).
11. Sun, T., Shrestha, E., Hamburg, S. P., Kupers, R. & Ocko, I. B. Climate impacts of hydrogen and methane emissions can considerably reduce the climate benefits across key hydrogen use cases and time scales. *Environ. Sci. Technol.* **58**, 5299–5309 (2024).
12. Patterson, J. D. Atmospheric history of H_2 over the past century reconstructed from South Pole firn air. *Geophys. Res. Lett.* **47**, 2020, e2020GL087787 (2020).
13. Patterson, J. D. et al. H_2 in Antarctic firn air: atmospheric reconstructions and implications for anthropogenic emissions. *Proc. Natl Acad. Sci. USA* **118**, e2103335118 (2021).
14. Derwent, R. G., Simmonds, P. G., O'Doherty, S. J., Manning, A. J. & Spain, T. G. A 24-year record of high-frequency, in situ, observations of hydrogen at the Atmospheric Research Station at Mace Head, Ireland. *Atmos. Environ.* **203**, 28–34 (2019).
15. Pétron, G. et al. Atmospheric hydrogen dry air mole Fractions from the NOAA GML Carbon Cycle Cooperative Global Air Sampling Network, 2009–2021. *NOAA GML CCGG Division*. Version 2023-07-05 https://doi.org/10.15138/WP0W-EZ08 (2023).
16. Seller, W. & Conrad, R. in *The Geophysiology of Amazonia* (ed. Dickenson, R.) 133–160 (Wiley, 1987).
17. Ehhalt, D. H. & Rohrer, F. The tropospheric cycle of H_2: a critical review. *Tellus B Chem. Phys. Meteorol.* **61**, 500–535 (2009).
18. Pieterse, G. et al. Reassessing the variability in atmospheric H_2 using the two-way nested TM5 model. *J. Geophys. Res. Atmos.* **118**, 3764–3780 (2013).
19. Yashiro, H., Sudo, K., Yonemura, S. & Takigawa, M. The impact of soil uptake on the global distribution of molecular hydrogen: chemical transport model simulation. *Atmos. Chem. Phys.* **11**, 6701–6719 (2011).
20. Yver, C. E. et al. A new estimation of the recent tropospheric molecular hydrogen budget using atmospheric observations and variational inversion. *Atmos. Chem. Phys.* **11**, 3375–3392 (2011).
21. Novelli, P. C. et al. Molecular hydrogen in the troposphere: global distribution and budget. *J. Geophys. Res.* **104**, 30427–30444 (1999).
22. Paulot, F. et al. Global modeling of hydrogen using GFDL-AM4.1: sensitivity of soil removal and radiative forcing. *Int. J. Hydrogen Energy* **46**, 13446–13460 (2021).
23. Paulot, F., Pétron, G., Crotwell, A. M. & Bertagni, M. B. Reanalysis of NOAA H_2 observations: implications for the H_2 budget. *Atmos. Chem. Phys.* **24**, 4217–4229 (2024).
24. Zhang, Z. et al. Anthropogenic emission is the main contributor to the rise of atmospheric methane during 1993–2017. *Natl Sci. Rev.* **9**, nwab200 (2021).
25. Xu, R. et al. Global N_2O emissions from cropland driven by nitrogen addition and environmental factors: comparison and uncertainty analysis. *Global Biochem. Cycles* **34**, e2020GB006698 (2020).
26. Zheng, B. Global atmospheric carbon monoxide budget 2000–2017 inferred from multi-species atmospheric inversions. *Earth Syst. Sci. Data* **11**, 1411–1436 (2019).
27. Hauglustaine, D. A. & Ehhalt, D. H. A. A three-dimensional model of molecular hydrogen in the troposphere. *J. Geophys. Res. Atmos.* **107**, ACH 4-1–ACH 4-16 (2002).
28. Sanderson, M. G., Collins, W. J., Derwent, R. G. & Johnson, C. E. Simulation of global hydrogen levels using a Lagrangian three-dimensional model. *J. Atmos. Chem.* **46**, 15–28 (2003).
29. Price, H. et al. Global budget of molecular hydrogen and its deuterium content: constraints from ground station, cruise, and aircraft observations. *J. Geophys. Res.* **112**, D22108 (2007).
30. Pieterse, G. et al. Global modelling of H_2 mixing ratios and isotopic compositions with the TM5 model. *Atmos. Chem. Phys.* **11**, 7001–7026 (2011).
31. Grant, A., Archibald, A. T., Cooke, M. C., Nickless, G. & Shallcross, D. E. Modelling the oxidation of 15 VOCs to track yields of hydrogen. *Atmos. Sci. Lett.* **11**, 265–269 (2010).
32. Rhee, T. S., Brenninkmeijer, C. A. M. & Röckmann, T. The overwhelming role of soils in the global atmospheric hydrogen cycle. *Atmos. Chem. Phys.* **6**, 1611–1625 (2006).
33. Bond, S. W., Gül, T., Reimann, S., Buchmann, B. & Wokaun, A. Emissions of anthropogenic hydrogen to the atmosphere during the potential transition to an increasingly H_2-intensive economy. *Int. J. Hydrogen Energy* **36**, 1122–1135 (2011).
34. Conrad, R. & Seiler, W. Contribution of hydrogen production by biological nitrogen fixation to the global hydrogen budget. *J. Geophys. Res. C Oceans* **85**, 5493–5498 (1980).
35. Chen, Q., Popa, M. E., Batenburg, A. M. & Röckmann, T. Isotopic signatures of production and uptake of H_2 by soil. *Atmos. Chem. Phys.* **15**, 13003–13021 (2015).
36. Williams, R. T. & Bainbridge, A. E. Dissolved CO, CH_4, and H_2 in the Southern Ocean. *J. Geophys. Res.* **78**, 2691–2694 (1973).
37. Schmidt, U. Molecular hydrogen in the atmosphere. *Tellus* **26**, 78–90 (1974).
38. Seiler, W. & Schmidt, U. in *The Sea: Ideas and Observations* Vol. 5. (ed. Goldberg, E. D.) 219–243 (Wiley, 1974).
39. Herr, F. L. & Barger, W. R. Molecular hydrogen in the near-surface atmosphere and dissolved in waters of the tropical North Atlantic. *J. Geophys. Res.* **83**, 6199–6205 (1978).
40. Moore, R. M., Punshon, S., Mahaffey, C. & Karl, D. The relationship between dissolved hydrogen and nitrogen fixation in ocean waters. *Deep Sea Res. I* **56**, 1449–1458 (2009).
41. Morfopoulos, C., Foster, P. N., Friedlingstein, P., Bousquet, P. & Prentice, I. C. A global model for the uptake of atmospheric hydrogen by soils. *Global Biogeochem. Cycles* **26**, GB3013 (2012).
42. Brown, M. A. J., Warwick, N. J. & Archibald, A. T. Multi-model assessment of future hydrogen soil deposition and lifetime using CMIP6 data. *Geophys. Res. Lett.* **52**, 2025, e2024GL113653 (2025).
43. Sander, S. P. et al. *Chemical Kinetics and Photochemical Data for Use in Atmospheric Studies Evaluation No. 15*. Report No. JPL-Publ-06-2 (NASA Panel for Data Evaluation, 2006).
44. Xiao, X. et al. Optimal estimation of the soil uptake rate of molecular hydrogen from the Advanced Global Atmospheric Gases Experiment and other measurements. *J. Geophys. Res. Atmos.* **112**, D07303 (2007).
45. Herridge, D. F., Giller, K. E., Jensen, E. S. & Peoples, M. B. Quantifying country-to-global scale nitrogen fixation for grain legumes II. Coefficients, templates and estimates for soybean, groundnut and pulses. *Plant Soil* **474**, 1–15 (2022).
46. Reis, C. R. G. et al. Biological nitrogen fixation across major biomes in Latin America: patterns and global change effects. *Sci. Total Environ.* **746**, 140998 (2020).
47. Chen, Y. et al. Multi-decadal trends and variability in burned area from the fifth version of the Global Fire Emissions Database (GFED5). *Earth Syst. Sci. Data* **15**, 5227–5259 (2023).
48. Sindelarova, K. et al. High resolution biogenic global emission inventory for the time period 2000–2019 for air quality modelling. *Earth Syst. Sci. Data* **14**, 251–270 (2022).
49. Gasser, T. et al. The compact Earth system model OSCAR v2.2: description and first results. *Geosci. Model Dev.* **10**, 271–319 (2017).
50. Ocko, I. B. & Hamburg, S. P. Climate consequences of hydrogen emissions. *Atmos. Chem. Phys.* **22**, 9349–9368 (2022).
51. IPCC. *Climate Change 2021: The Physical Science Basis. Contribution of Working Group I to the Sixth Assessment Report of the Intergovernmental Panel on Climate Change* (eds Masson-Delmotte, V. et al.) (Cambridge Univ. Press, 2021).
52. Bauer, N. et al. Shared socio-economic pathways of the energy sector – quantifying the narratives. *Global Environ. Change* **42**, 316–330 (2017).
53. Momeni, A. et al. Quantification of hydrogen emission rates using downwind plume characterization techniques. *Environ. Sci. Technol.* **59**, 6016–6024 (2025).
54. Worman, S. L., Pratson, L. F., Karson, J. A. & Schlesinger, W. H. Abiotic hydrogen (H_2) sources and sinks near the Mid-Ocean Ridge (MOR) with implications for the subseafloor biosphere. *Proc. Natl Acad. Sci. USA* **117**, 13283–13293 (2020).
55. Zgonnik, V. The occurrence and geoscience of natural hydrogen: a comprehensive review. *Earth Sci. Rev.* **203**, 103140 (2020).
56. Meredith, L. K. et al. Ecosystem fluxes of hydrogen in a mid-latitude forest driven by soil microorganisms and plants. *Glob. Chang. Biol.* **23**, 906–919 (2017).
57. Gorgolewski, A. S., Caspersen, J. P., Vantellingen, J. & Thomas, S. C. Tree foliage is a methane sink in upland temperate forests. *Ecosystems* **26**, 174–186 (2023).
58. Gauci, V. et al. Global atmospheric methane uptake by upland tree woody surfaces. *Nature* **631**, 796–800 (2024).
59. Ciais, P. et al. Definitions and methods to estimate regional land carbon fluxes for the second phase of the REgional Carbon Cycle Assessment and Processes Project (RECCAP-2). *Geosci. Model Dev.* **15**, 1289–1316 (2022).

Methods

Chemical oxidation of CH_4

The H_2 production rate from the chemical oxidation of CH_4 was estimated based on its temperature-dependent reaction rates with OH (ref. 60), which produces HCHO that subsequently forms H_2 through further photolysis (Supplementary Note 3). We ignored H_2 produced from the CH_4 + O one-dimensional reaction pathway[61,62], which accounts for less than 5% of CH_4 loss in the atmosphere[63].

The overall fraction of H_2 produced in the global CH_4 reaction chain can be calculated for each time step as

$$P_{CH_4:H_2} = \int k_1(T) \times [OH] \times [CH_4] \times F_{H_2} \quad (1)$$

where $k_1(T)$ is the temperature-dependent reaction rate between CH_4 and OH, F_{H_2} is the total yield factor of H_2 within the whole chain, and [OH] and [CH_4] are the tropospheric OH and CH_4 concentrations, respectively. $P_{CH_4:H_2}$ is usually simplified by applying a global mean of [OH], k_1(T), [CH_4] and F_{H_2} in previous studies[17,21], which can lead to large uncertainty and bias because a large variation of the global mean must be included, considering the inhomogeneous distribution of the chemical species and the reaction rates. Here, we improved the estimation by considering spatial distribution and temporal variations of H_2 production from CH_4 oxidation using available data from data assimilation and atmospheric chemistry model simulations. The $P_{CH_4:H_2}$ was estimated by integrating global grids with a spatial resolution at 3.75° (longitude) × 1.875°(latitude) and a temporal resolution of 3 h (3-D), which substantially reduced the uncertainty of our estimates.

The 3-D distribution of $k_1(T)$ was estimated using the temperature field from ERA-Interim reanalysis meteorology data[64]. We used eight [OH] fields and three [CH_4] fields to produce 24-member estimates to obtain an ensemble-based mean estimate. The eight [OH] fields were obtained from the INVAST model and seven CMIP6 (refs. 65,66) models: CESM2-WACCM (ref. 67), EC-Earth3-AerChem (ref. 68), GISS-E2.1-G (ref. 69), GISS-E2.1-H (ref. 70), GISS-E2.2-G (ref. 71), MPI-ESM-1.2-HAM (ref. 72) and MRI-ESM2.0 (ref. 73). For the CMIP6 runs, we used the historical simulations that cover 1990–2014 supplemented with the SSP3-70 scenario simulation for the 2015–2020 period. The SSP3-70 scenario simulation did not consider the impact of COVID-19 on OH changes 2020, which was corrected using change ratios from INVAST. The three 3D distributions of tropospheric CH_4 were produced by atmospheric transport models after surface measurement assimilation, which are CIF-LMDz (ref. 74), MIROC4-ACTM (ref. 63) and NISMON (ref. 75), respectively. The 3D F_{H_2} was computed based on the reaction chain, in which grid level values range from 0.25 to 0.7 and global mean ranges from 0.41 to 0.43 (Supplementary Note 3).

We found that our ensemble of OH fields overestimates CH_4 oxidation, yielding a global mean oxidation of 517 Tg CH_4 yr^{-1} over 2007–2018, compared with the IPCC AR6 top-down estimate of 472 Tg CH_4 yr^{-1}. Furthermore, our ensemble underestimates the uncertainty associated with OH-driven CH_4 oxidation (about 8%) and H_2 production (about 10%) when compared with the approximately 11% uncertainty in CH_4 lifetime reported in AR6. Notably, our estimate is bottom-up, and the tendency of bottom-up models to overestimate oxidation fluxes is well-documented[51], which is one reason why IPCC AR6 prioritizes top-down values for CH_4 budget assessments. To reconcile these differences, we corrected the H_2 production from CH_4 oxidation by scaling our bottom-up H_2 fluxes to match the AR6 CH_4 oxidation value. Specifically, we applied a constant scaling factor of 472/519 ≈ 0.913 to the H_2 production from CH_4 oxidation.

To propagate the uncertainty in CH_4 oxidation into the H_2 production estimate, we estimated the new standard deviation (SD) as

$$SD'_{H_2-production} = \mathrm{sqrt}\left(\left(\frac{SD_{H_2-production}}{SD_{CH_4\ oxidation}}\right)^2 + \left(\frac{SD_{IPCC\ CH_4\ lifetime}}{Mean_{IPCC\ CH_4\ liftime}}\right)^2\right) \quad (2)$$

where $SD'_{H_2-production}$ is the new SD for H_2 production from CH_4–OH oxidation, $SD_{H_2-production}$ is the old SD for H_2 production from CH_4–OH oxidation and $SD_{CH_4\ oxidation}$ is the SD for oxidized CH_4 through reacting with OH estimated using our ensemble of OH and CH_4 fields. $SD_{IPCC\ CH_4\ lifetime}$ and $Mean_{IPCC\ CH_4\ liftime}$ are taken from IPCC AR6, which are 1.1 years and 9.7 years, respectively.

Oxidation of NMVOC

NMVOCs are more reactive than CH_4, and their chemical reaction chains to produce H_2 are also more complicated and less understood. Moreover, estimates of precursor NMVOC emissions for many species are more uncertain than for CH_4 because the emissions are smaller than CH_4 and the sources are less clear. Owing to these uncertainties, the estimates of their contribution to the global production of H_2 are more difficult and uncertain. We adopted global emission data of NMVOC from a few recently improved dataset[76–78] (Supplementary Notes 4 and 5) to estimate H_2 production from the oxidation of NMVOC.

We used the method in ref. 21, later adopted in ref. 17. Briefly, the global production rate of H_2 from the oxidation of a given species of NMVOC can be approximated by

$$\underline{P_{NMVOC_i,H_2}} = S_i \times \underline{Y_i} \times \underline{F'_{H_2}} \times (m_{H_2}/m_C) \quad (3)$$

where S_i is the global emission rate of $NMVOC_i$ in Tg C yr^{-1}, $\underline{Y_i}$ is the global average yield of HCHO per carbon atom in $NMVOC_i$. $\underline{F'_{H_2}}$ is the average fraction of HCHO that forms H_2, which is 0.31 ± 0.1 (ref. 17), m_{H_2}/m_C is the mass ratio between hydrogen and the carbon atom, that is, ⅙. We adopted $\underline{Y_i}$ that is compiled based on refs. 17,21,31 (Supplementary Note 6).

The most important NMVOCs for H_2 production are isoprene (C_5H_8), monoterpenes ($C_{10}H_x$) and methanol (CH_3OH), mostly from biogenic sources. We, therefore, provided an estimate of H_2 production from biogenic isoprene, monoterpenes and methanol individually, and for all other minor biogenic NMVOCs collectively. We used CAMS-GLOB-BIO v.3.1, v.3.0 and v.1.2 (refs. 48,79), MEGAN_MACC (ref. 79) and MEGAN v.3.2 (ref. 80) as our main datasets to obtain global total and gridded biogenic NMVOC emissions (Supplementary Note 4).

We also consider H_2 production from the oxidation of NMVOCs released from biomass burning and anthropogenic sources. The total NMVOC emission from wildfires is estimated using NMVOC emission factors computed based on species-level emission factors reported in ref. 81 and databases of grand total dry biomass burnt in different categories (Supplementary Note 5).

The total other anthropogenic NMVOC from fossil fuel combustion, biofuel combustion and other processes were acquired from three datasets. The three datasets are the widely used Emission Database for Global Atmospheric Research (EDGAR) v.8.1 (ref. 82), Community Emissions Data System (CEDS) v_2021_11_25 (ref. 77) and ECLIPSE v.6b (ref. 83) (Supplementary Note 5).

To cross-validate our estimate of total photochemical sources of H_2, we also used a second method based on satellite-observed formaldehyde (HCHO) (ref. 26) to estimate total H_2 production rates from photochemical oxidation (Supplementary Note 7). Both estimates show a similar increasing trend (r = 0.87) during 2005–2017, and both estimates are similar (40.5 ± 5.1 Tg yr^{-1} compared with 38.6 ± 1.6 Tg yr^{-1}) during the common period 2008–2017.

Given that not all biogenic and fire NMVOC emission datasets provided data before 2000, we used a reduced number of datasets for the period 1990–2000 to ensure a complete three-decade series estimate. For biogenic NMVOC emissions, we used the single MEGAN_MACC

dataset for years before 2000, but we scaled the data with a constant so its 2010–2020 mean equals the 2010–2020 ensemble mean based on all biogenic emission datasets. For fire emissions, we used the historic global biomass burning emissions for CMIP6 (BB4CMIP)[84] before 2003 and again scaled it with a constant number making its 2010–2020 mean equal to the 2010–2020 mean based on the ensemble fire emission datasets.

Fossil fuel combustion

Incomplete combustion of fossil fuel produces CO, which in direct exhaust can produce H_2 through the water–gas shift reaction:

$$CO + H_2O \Longleftrightarrow CO_2 + H_2 \quad (4)$$

Although CO emission factors from fossil fuel combustions are known from a range of measurements, there are few measurements of H_2 emission factors. However, equation (4) suggests that the production of H_2 and CO are tightly coupled. Therefore, H_2 emissions from fossil fuel combustion were estimated by scaling against the better-known CO emissions, using H_2/CO emission ratios for different processes. We determined H_2/CO emission ratios from a few sources for different sectors of fossil fuel usage (Supplementary Note 8).

The global amounts of CO emissions were obtained from the widely used and latest version of the EDGAR v.8.1 (ref. 85), the CEDS v_2024_11_25 (ref. 86) and the Greenhouse Gas–Air Pollution Interactions and Synergies (GAINS ECLIPSE v.6b) (ref. 83).

Biomass combustion

We estimated direct H_2 emission from biomass combustion, including wildfires and biofuels. For wildfires, we estimated the H_2 emission using emission factors reported in ref. 81 and the total amount of dry matter burnt by different combustion types from the latest version of four widely used database inventories: Fire Inventory from NCAR (FINN), Global Fire Emission Database (GFED), Quick Fire Emission Dataset (QFED) and Global Fire Assimilation System (GFAS). The uncertainty in our estimate considered both the spread among different estimates of burnt dry matter and uncertainty around emission factors (Supplementary Note 5). None of these fire datasets provided data before 2000, and some started in 2003. Therefore, we used the historic global biomass burning emissions for CMIP6 (BB4CMIP)[84] before 2003 and scaled it with a constant number making its 2010–2020 mean equal to the 2010–2020 mean based on the ensemble fire emission datasets to obtain a complete time series for 1990–2020.

For biofuel, similarly as for fossil fuels, we used CO emissions from the latest version of the Emission Database for Global Atmospheric Research (EDGAR_81) (ref. 85), the Community Emissions Data System (CEDS v_2024_11_25) (ref. 86) and the Greenhouse Gas–Air Pollution Interactions and Synergies (GAINS ECLIPSE v.6b) (ref. 83). Only CEDS v_2024_11_25 has separated the emission from biofuels and fossil fuels. We, therefore, applied the same ratios of emission of CO from biofuels and fossil fuels in the same sectors from CEDS v_2024_11_25 to the other two datasets. We then used the H_2 to CO emission ratios compiled from the latest literature (Supplementary Note 8) to estimate H_2 emissions.

Leakage from H_2 production

At present, the average global leakage rate for H_2 production and distribution is relatively unconstrained. Rare measurements have been taken for the losses of gaseous H_2 from its production and distribution. A previous study[87] reported that losses of gaseous H_2 are less than 1%, whereas those of liquid H_2 are of the order of 1–10% based on a distribution grid in Germany. Another study[33] used a total loss rate range of 1–4% for 2010. Because we estimate only the H_2 leakage from production, we adopted a leakage rate based on several studies: (1) the Frazer–Nash Consultancy estimated an H_2 leakage rate of 0.5% in the process of production[88]; (2) ref. 89 reported grey hydrogen production based on steam methane reforming could have a less than 1% total leakage rate; (3) ref. 90 estimated the leakage rate from blue hydrogen production to be approximately 1.5% based on a combination of natural gas leakage data and what is known about the correlation between hydrogen leakage properties and those of natural gas; (4) venting and fugitive losses often happen for natural gas production and processing; yet its leakage rate of natural gas ranges from about 0.6% (ref. 91) to about 1.45% (ref. 92). Therefore, in this study, we adopt a 1 ± 0.5% leakage rate for production.

Global production of H_2 has more than tripled since 1975 (ref. 93) and will continue to rise. We take the global total demand of H_2 from IEA[93] (Supplementary Note 9), because the total production of H_2 equals its total consumption. We linearly interpolated the total production of H_2 for years not reported in IEA between 1990 and 2020[93].

H_2 from biological nitrogen fixation

Using the direct measurement of H_2 release from clover fields, a previous study[34] estimated a global emission of H_2 from N fixation in land at 2.4–4.9 Tg yr^{-1}, which forms the basis for most later bottom-up estimates[17,21,27,28]. This source may have changed with time, for instance, because of land use and land cover changes such as cropland expansion and deforestation. To obtain a new estimate for our study period, we searched simulated outputs from models that participated in TRENDY v.10 or v.11 (ref. 94) (trends in the land carbon cycle) and obtained grid-based nitrogen fixation rates from eight TRENDY models (Supplementary Note 10). We assumed a constant ratio between H_2 production and nitrogen fixation across different land cover types. We then applied the ratios of 0.032 ± 0.02, according to the nitrogen fixation rate and hydrogen production rate measured in clover fields[34] and potted peanuts (Supplementary Notes 11 and 17).

Estimates of global H_2 source from the oceans were carried out before by extrapolating site-measured H_2 concentration to global oceans and applying the film model, which ranges from 2 Tg H_2 yr^{-1} to 4 Tg H_2 yr^{-1} because of different assumptions of H_2 solubility in seawater[17]. These early estimates were lower than later estimates that are based on global oceanic N fixation rate, mainly because early measurements of H_2 concentration were mainly in the North and South Atlantic and missed the Pacific, which seems to have much higher N_2 fixation rates[17]. The recent estimate of H_2 emission from N_2 fixation rate assumes that the main part of H_2 in oceanic water must come from nitrogen fixation by cyanobacteria. Specifically, ref. 29 estimated a global H_2 emission from the oceans of 6 Tg H_2 yr^{-1}, based on a global oceanic N_2 fixation rate of 150 Tg N yr^{-1}, a stoichiometry of 1:1 for the moles of H_2 produced per mole of N_2 and an internal H_2 loss rate of 0.45 (that is, a H_2/N_2 net production ratio at 0.55). We refined the oceanic source estimate of H_2 by applying a similar methodology with updated global microbial N fixation data and new H_2/N_2 net production estimates derived from both field and laboratory incubation measurements. Based on a few contemporary estimates[95–98] of global total marine fixation that is constrained by in situ measures, we adopted a total marine N fixation of 160 ± 60. To obtain a time series estimate from 1990 and a spatial estimate, we have obtained oceanic N fixation data from the NEMO-PlankTOM model and scaled the model data to make its 2010–2020 total N fixation equal to 160 Tg N yr^{-1}. Although studies remain limited, we compiled a net H_2/N_2 production ratio of 0.43 ± 0.2 from a few recent studies (Supplementary Note 11).

Other minor sources

There are other minor sources of H_2, which, when added together, are not negligible. One well-known source of H_2 is from geological origins such as emissions from volcanoes, surface gas seeps, hot springs, mining sites, and oil and gas wells[55]. A previous study[55] estimated the total geological origin of natural hydrogen of 23 ± 8 Tg H_2 yr^{-1}. This number is not adopted here because (1) it is too large to provide a useful constraint on our H_2 budget and (2) a large part of it is deep oceanic sources (mid-oceanic rifts, oceanic crust serpentinization, the basaltic layer

of oceanic crust and so on), which may hardly vent through the water surface and make it into the atmosphere. For the natural geologic origin of H_2 sources, we consider only volcanic emissions. Another study[99] made an early estimate of the average emission rate of 0.2 Tg H_2 yr^{-1}. Later, ref. 100 estimated 0.24 Tg H_2 yr^{-1} for just subaerial volcanoes. Recently, ref. 101 estimated that the emission rate is 0.18–0.69 Tg H_2 yr^{-1} for subaerial volcanoes and 0.02–0.05 Tg H_2 yr^{-1} for mid-ocean ridge volcanoes. Combining these data sources, we estimate the emission rate of H_2 from volcanoes as 0.32 ± 0.1 Tg H_2 yr^{-1}.

Fermentation processes in waterlogged soils and the digestive tracts of animals release both methane and hydrogen. Although there are many studies on the emission rate of methane, rare data and research can be found on hydrogen. A previous study[102] measured an H_2/CH_4 emission ratio of 0.008 mol mol^{-1} in the flooded freshwater wetland; another study[103] measured a H_2/CH_4 emission ratio of 0.0098 mol mol^{-1} and 0.005 mol mol^{-1} at two rice fields in Beijing and Guangzhou, China, respectively; and ref. 104 also reported an H_2/CH_4 ratio in a rice paddy at 0.006 mol mol^{-1}. Using this sparse information, we adopt an average of 0.007 mol mol^{-1} H_2/CH_4 emission ratio and assume it is the same for similar systems, including paddy rice, landfills and waste treatment, and wetlands, which are estimated to have global CH_4 emission as 32 [25–37] Tg CH_4 yr^{-1}, 69 [56–80] Tg CH_4 yr^{-1} and 159 [119–203] Tg CH_4 yr^{-1}, respectively, during 2010–2020. Combining these data, we estimate a total H_2 emission of 0.23 ± 0.05 Tg H_2 yr^{-1} for these fermentation systems. Similar methods were used to estimate emissions from enteric fermentation in livestock and wild animals. There are some, but not many, measurements of H_2/CH_4 emission from livestock. We have collected these measurements (Supplementary Note 12) and adopted a median value of 0.022 mol mol^{-1}, which is slightly higher than the value used in ref. 17 based on no real measurement of emission. Some wild animals have a fermentation process occurring in their rumen similar to domesticated livestock and, therefore, can produce CH_4 and H_2 too. Manures are found to produce H_2 as well[105]. The same H_2/CH_4 ratio is assumed for ruminant emissions from other wild animals and manure management due to a lack of data. The Global Carbon Project estimated 112 [107–118] Tg CH_4 yr^{-1} for livestock and manure management and 2 [1–3] g CH_4 yr^{-1} for wild animals during 2010–2020 (ref. 106). Using this information, we estimate the total global H_2 production from livestock production and wild animals as 0.31 ± 0.1Tg H_2 yr^{-1}.

Termites are also important H_2 emitters from fermentation, as pointed out very early in ref. 107. We estimate the H_2 emissions from termites also based on the reported H_2/CH_4 emission ratios[108–111] (Supplementary Note 12). These studies measured H_2/CH_4 emission ratio from various termite species with varying diets, and we adopted the median value of 1.2 mol mol^{-1}. Adopting the global CH_4 emission of 10 [4–16] Tg CH_4 yr^{-1} during 2010–2020 from the Global Methane Budget[106], we estimated H_2 emission from termites at 1.5 ± 0.9Tg H_2 yr^{-1}.

Human breath contains varying amounts of H_2 as suggested by the clinic breath test. Assuming an average of 25 ppm H_2 from human breath[17] and an average breathing rate of about 11 kg air day^{-1} for a human being, we estimate the total release of H_2 from humans as 0.048 Tg yr^{-1} based on an average global population of 7.37 billion during 2010–2020.

There are two other minor volume photochemical sources identified, that is, the oxidation of ozone (O_3) and glyoxal (CHOCHO) (Supplementary Note 13). The yielding rate of H_2 from photolysis of O_3 has been measured to be 1 [0, 1.5]% (ref. 112) and 0.6 [0, 1.3]% (ref. 113). We thus adopted a median rate of 0.7 ± 0.7. A previous study[114] estimated the total chemical loss of O_3 at 4,360 Tg yr^{-1} for recent years using the latest GEOS-Chem chemical transport model combined with advanced satellite, aircraft and ground station observations. Out of this, 51% (ref. 114), that is, 2,180 Tg, is lost through the photolysis path (Supplementary Note 13) that produces H_2. Using these data, we directly estimate the global production of H_2 from O_3 oxidation as 0.64 ± 0.64 Tg H_2 yr^{-1}. Glyoxal is mainly formed in the oxidation of VOC, similar to the production of HCHO through VOC oxidation. The global source of glyoxal is about 48 ± 8 Tg yr^{-1} (refs. 115–117). Also, the yielding rate of H_2 of glyoxal oxidation (equation (R3b) in Supplementary Note 13) equals that of HCHO oxidation (equation (R3) in Supplementary Note 3). Adopting the yielding rate of the HCHO process of H_2 production at 0.65 ± 0.15×0.6 ± 0.1 (ref. 17), we estimate an H_2 production of 0.65 ± 0.2 Tg H_2 yr^{-1}.

Reaction with OH

H_2 can be removed from the atmosphere by reaction with OH:

$$H_2 + OH \rightarrow H_2O + H \quad (5)$$

The global loss of H_2 by this reaction can be estimated by integration over a 3D space:

$$L_{H_2:OH} = \int k_5(T) \times [OH] \times [H_2] \quad (6)$$

where, the temperature-dependent reaction rate ($k_5(T) = 2.8 \times 10^{-12} \times \exp(-1{,}800/T)$ mol^{-1} cm^3 s^{-1}) is estimated using the ERA-Interim reanalysis meteorology data[64], and the [OH] is taken from model-simulated 3D [OH] fields, as mentioned earlier. We used our 3D distribution of H_2 produced through kriging interpolation (Supplementary Note 1). The same scaling and uncertainty propagation approach used for estimating H_2 production from CH_4 oxidation was also applied here to scale H_2 loss from its reaction with OH and adjust the corresponding uncertainties.

Soil uptake

There is plenty of evidence for uptake of H_2 in soils containing organic carbon from observations in both the laboratory and the field[41,118]. A mini review of previous studies of soil H_2 uptake was provided in Supplementary Note 14.

We adopted the process-based model developed in ref. 41 as the main model to estimate the monthly deposition rates from 1992 to 2020. Details of this model can be found in ref. 41.

To also account for the uncertainty in estimating soil properties that influence hydrogen uptake velocities, soil data of the top layer (about 10 cm depth) were obtained from simulations of a group of dynamic global vegetation models. These models include eight models that participated in TRENDY v.10 project[94], as contributions to the Global Carbon Budget 2021 (ref. 119) and another two models—SPLASH (simple process-led algorithms for simulating habitats)[120] and the global land data assimilation system (GLDAS) reanalysis data. The eight TRENDY dynamic global vegetation models are LPX-BERN, JULES, ORCHIDEE, CABLE-POP, VISIT, JSBACH, CLASSIC and CLM5.0, which account for various soil characteristics to simulate land–atmosphere flux. We used both the input soil parameters, including the clay fraction of soil, sand fraction of soil and total soil porosity of these models, as well as simulated monthly soil temperature, soil moisture and snow depths. An exception is SPLASH because the current version could not properly simulate soil temperature, and we used GLDAS soil temperature instead.

To account for uncertainties arising from different parameterizations, we considered another six additional parameterizations (Supplementary Note 15). These include (1) adopting the diffusion scheme used in refs. 19,22,121; (2) adding the effect of dry top layers acting as a diffusion barrier, following ref. 122; (3) instead of using net productivity or Normalized Difference Vegetation Index to constrain H_2 deposition velocities, adapting the scheme from ref. 22 that using soil carbon content to constrain; (4) adopting the scheme of soil moisture content regulation from ref. 122; (5) Changing the maximum biological uptake (k_{max}) to a low bound value (0.01226 s^{-1}) based on measurement in ref. 123 and a high value (0.1 s^{-1}) derived from ref. 122. A previous study[124] developed a new parameterization on soil moisture regulation of $k_{max,}$ using a function on soil water potential with an activation threshold at the wilting point. We did not include it because the required values for soil-type-specific coefficients provided in ref. 124 shall not

be directly used for TENDY soil products, as their soil texture or types may be different from those used in that paper to derive those values. With an ensemble of 10 models for simulating soil properties, this parameterization is difficult to apply because the coefficient values must be re-derived for different soil types across different models.

In summary, we estimated an ensemble of monthly H_2 deposition velocities using 10 sets of soil inputs and seven model parameterizations for modelling H_2 deposition velocities, resulting in a total of 70 model runs. Applying the observed H_2 mixing ratio in the atmosphere (Supplementary Note 1) to these deposition velocities, we then estimated an ensemble H_2 uptake rate by soil.

Hydrogen climate impact

Increasing atmospheric H_2 leads to indirect climate impacts, and its future concentration and climate impact will depend on how both sources and sinks change over time.

To estimate the climate impact of changing H_2 concentrations in the future H_2 economy, we used v.4.0-alpha-1 of the compact Earth system model OSCAR to simulate the CH_4–H_2 system. We updated the published OSCAR v.3.3 (ref. 125) with three key changes: updated tropospheric and stratospheric lifetimes of all non-CO_2 greenhouse gases, updated radiative forcing of short-lived species (aerosols and ozone) and the inclusion of the H_2 biogeochemical cycle. The integration of H_2 biogeochemical cycle into OSCAR covers two aspects: the representation of the H_2 cycle and budget, and the integration of its impact on tropospheric OH lifetimes (which feed back on species affected by OH such as CH_4) and on the effective radiative forcing of ozone and stratospheric water vapour (direct impact of H_2 and indirect impact through changes in CH_4). The detailed description of the model is provided in Supplementary Note 16.

To isolate the contribution of H_2 to climate change and avoid too many interactions in the Earth system, we isolate the CH_4 and H_2 cycles and their interactions by prescribing the atmospheric concentrations of all other greenhouse gases (CO_2, N_2O and 48 halogenated compounds) to the model. We also prescribed the effective radiative forcings from forcers that are not directly related to the CH_4–H_2 system in the model (all aerosols, aviation-induced cloudiness, light-absorbing particles on snow, albedo from land use change, stratospheric volcanic aerosols and solar activity). The resulting system describes the evolution of atmospheric CH_4, atmospheric H_2, stratospheric water vapour and tropospheric and stratospheric O_3, as well as the global climate change induced by these forcers and the prescribed ones. Apart from the atmospheric concentrations and effective radiative forcings listed above, the resulting model is driven by time series of anthropogenic and biomass burning emissions of H_2, CH_4, NO_x, CO and VOCs.

Using time series forcing data (Supplementary Note 16), we simulated past and future changes in the CH_4–H_2 system to estimate the climate impact of hydrogen. Several sets of preliminary simulations, including both concentration-driven and climate-driven scenarios, were conducted over the historical period to assess the ability of the model to reproduce the evaluated budget and to estimate any budget imbalance through mass conservation. These were performed before the main simulation. The main simulation is emission-driven for both the historical and future periods, in which we incorporated previously diagnosed missing fluxes from unrepresented processes to accurately reproduce reconstructed historical atmospheric concentrations. This main simulation was then compared with a counterfactual scenario in which atmospheric H_2 levels were fixed at preindustrial values, allowing us to quantify the climate impact of the lack of representation of H_2 in climate projections.

The H_2-cycling-related input data for historical and future simulations are either based on or constrained by our budget (Supplementary Note 16). For future simulations, we consider only a few typical warming scenarios, that is, different marker SSP scenarios (SSP5-85, SSP4-60, SSP4-34, SSP2-45, SSP1-26 and SSP1-19; SSP3 is excluded as no hydrogen-related variable was reported). The scenarios provide projections of the concentrations and emissions of CH_4, NO_x, CO, VOCs and other gases needed for our climate model, as well as the total usage of H_2. To estimate projected H_2 concentrations in these SSP scenarios, H_2 emissions excluding leakage are derived from precursor emissions (for example, CO, CH_4 and NMVOCs) in the same way as for the historical period and scaled to match our 2020 estimates. The H_2 leakage was estimated by combining future H_2 usage data from the IPCC AR6 database and possible hydrogen leakage rates.

As more hydrogen is used in the economy, the production methods and uses of hydrogen will evolve, altering the extent and likelihood of hydrogen leakage. Future consumption of hydrogen is likely to be more distributed, for instance, in vehicles or blended into pipeline gas, and will no longer be mostly co-located with the production sites. Hydrogen end uses will be more diverse, involving sections such as blending with natural gas, iron and steel, electricity generation, road transport, chemical synthetic fuels, refineries, shipping and aviation, and buildings. Furthermore, the production technology of H_2 is also likely to evolve, with more hydrogen being green hydrogen instead of grey and blue hydrogen. All these factors will contribute to varying leakage rates in the future and H_2 is generally considered more prone to leakage than CH_4 because of its smaller molecule size unless specific mitigation measures are implemented. However, as mentioned above, there is still limited empirical data available to constrain the estimate of future leakage rates. Reported leakage rates across different components of the hydrogen value chain vary substantially—from as low as 0.0001% to as high as 20% (refs. 126,127). However, the average economy-wide leakage rates are expected to be less extreme[10,127]. Following the most recent studies on assessing the climate benefits of H_2 (refs. 3,11,50,128), we adopted an economy-wide hydrogen leakage range of 1–10%.

Uncertainties and limitations

Our analysis and synthesis of H_2 fluxes are based on a range of bottom-up inventories and models, subject to various uncertainties and limitations. First, many process-based models are used, including those for modelling H_2 directly (for example, the soil uptake model), for modelling input data to the H_2 model (for example, the TRENDY models) and for modelling precursor species and activities (for example, the models for estimating NMVOC emissions and the NEMO-PlankTOM ocean model for estimating BNF). These models include uncertainty associated with differences in model configuration as well as process parameterization, although the same forcings are applied to the same group of models to reduce variation among models (for example, TRENDY models). Second, inventories of precursor gases (for example, CH_4 and CO) include uncertainties originating from the underlying statistical activity data and emission factors they are based on refs. 77,129, regardless of the tiered approach used. These uncertainties contribute to our estimate of H_2 flux. For instance, waste management and solid biomass combustion are hard to track, partially because of informal and small-scale consumption or applications, leading to high uncertainty in the estimate of CH_4 and CO emissions and, therefore, related H_2 emissions. Last, there are limitations associated with the H_2 emission and yield factors because of limited measurement and variation among sources and regions. We used global and time constant H_2 yield factors from NMVOC and emission factors for transportation. However, these factors could vary across space and time because of different atmospheric or technological conditions, among NMVOC species, and among different types of vehicles. As more empirical data become available, a more detailed and comprehensive treatment of these emission and yield factors shall be needed to improve the estimate. Although we did not optimize any sink/source terms as in top-down inversion studies, top-down estimates were still used for constraining some terms. One maximal biological uptake value (that is, 0.038 s^{-1}) was tuned to match the global mean soil update from a top-down estimate[41], whereas two others were derived from an experiment or a soil

moisture parameterization scheme to reduce this dependence. Our 3D CH_4 concentrations were obtained from top-down inversions, and our CH_4 and OH oxidation terms were calibrated to match top-down CH_4 oxidation estimates. This dependence could be alleviated in the future through reliable measurements of the maximal biological uptake rate and the development of more consistent, better constrained OH fields.

In this study, we try to track and quantify the propagated uncertainties as much as possible, but we acknowledge that we could not include all sources of uncertainty. We collect as much activity data as possible, precursor gas emission data and emission factors. Our estimate of H_2 sink/sources was then based on the mean value of these ensemble collections, and the ensemble standard deviation was used to represent the uncertainty of the estimate. The uncertainty estimate in terms of standard deviation in our analysis includes all levels of uncertainties: (1) uncertainty of each single data source of activity or precursor gas emission if it is available; (2) variation among different data sources for each activity type or precursor gas species; (3) variation among emission factors for both precursor gas and H_2 when a collection of measurements is available; (4) different model input data and parameterization in case of process modelling (that is, the soil H_2 uptake modelling). When adding terms (that is, different inventories of gas emissions), the resulting standard deviation is computed as the square root of the sum of variances of all terms, assuming each term is normally distributed and independent. When multiplying terms, Monte Carlo simulations are applied in R language to compute the final standard deviation.

Data availability

Anthropogenic emission data: CEDS data are available from https://aims2.llnl.gov/search/input4MIPs/, EDGAR v.8.1 is available from https://edgar.jrc.ec.europa.eu/dataset_ap81/, ECLIPSE v.6b is available from https://iiasa.ac.at/models-tools-data/global-emission-fields-of-air-pollutants-and-ghgs/. Fire burning and emission data: GFED is available from https://www.globalfiredata.org/, FINN is available from https://rda.ucar.edu/datasets/d312009/, GFAS is available from ECMWF at https://www.ecmwf.int/en/forecasts/dataset/global-fire-assimilation-system, and QFED is available from https://ftp.as.harvard.edu/gcgrid/data/ExtData/HEMCO/QFED/v2018-07/. CMIP6 fire data is obtained from https://aims2.llnl.gov/search/input4MIPs/. Biogenic VOC emission data: MEGANv3.2 VOC is obtained from https://www.scidb.cn/en/detail?dataSetId=f1cdb0cfbd70410d88f491a75844912b, and CAMS-GLOB-BIOv1.2, CAMS-GLOB-BIOv3.0, CAMS-GLOB-BIOv3.1, and MEGAN-MACC are obtained from https://eccad.aeris-data.fr/. OH fields and CH_4 fields: INVAST OH Fields can be requested from Didier Hauglustaine, other seven CMIP6 OH fields are available from https://aims2.llnl.gov/search/input4MIPs/, The three CH_4 fields can be requested from Marielle Saunois and Prabir K. Patra. Soil attributes: GLDAS data are available from https://ldas.gsfc.nasa.gov/gldas, and TRENDY model data are obtained from individual modelers and also partially available at https://mdosullivan.github.io/GCB/. Different emission factors are summarized in Supplementary Information, and the gridded H_2 sinks and sources data produced in this study is available at Zenodo (https://zenodo.org/records/17162658). Figure 2 is created using Adobe Illustrator. Source data are provided with this paper.

Code availability

The OSCAR compact Earth system model code is available at Zenodo[125] (https://zenodo.org/records/10548477), whereas other analysing and modelling code can be required from the leading authors.

60. Bonard, A., Daële, V., Delfau, J.-L. & Vovelle, C. Kinetics of OH radical reactions with methane in the temperature range 295–660 K and with dimethyl ether and methyl-*tert*-butyl ether in the temperature range 295–618 K. *J. Phys. Chem. A* **106**, 4384–4389 (2002).
61. Jayanty, R. K. M., Simonaitis, R. & Heicklen, J. H_2 formation in the reaction of $O(^1D)$ with CH_4. *Int. J. Chem. Kinet.* **8**, 107–110 (1976).
62. Greenberg, R. I. & Heicklen, J. The reaction of $O(^1D)$ with CH_4. *Int. J. Chem. Kinet.* **4**, 417–432 (1972).
63. Chandra, N. et al. Emissions from the oil and gas sectors, coal mining and ruminant farming drive methane growth over the past three decades. *J. Meteorol. Soc Jpn II* **99**, 309–337 (2021).
64. Dee, D. P. et al. The ERA-Interim reanalysis: configuration and performance of the data assimilation system. *Quart. J. Roy. Meteor. Soc.* **137**, 553–597 (2011).
65. O'Neill, B. C. et al. The Scenario Model Intercomparison Project (ScenarioMIP) for CMIP6. *Geosci. Model Dev.* **9**, 3461–3482 (2016).
66. Eyring, V. et al. Overview of the Coupled Model Intercomparison Project Phase 6 (CMIP6) experimental design and organization. *Geosci. Model Dev.* **9**, 1937–1958 (2016).
67. Danabasoglu, G. *NCAR CESM2-WACCM Model Output Prepared for CMIP6* CMIP (Earth System Grid Federation, 2019).
68. EC-Earth Consortium (EC-Earth). *EC-Earth-Consortium EC-Earth3-AerChem Model Output Prepared for CMIP6 CMIP* (Earth System Grid Federation, 2020).
69. NASA Goddard Institute for Space Studies (NASA/GISS). *NASA-GISS GISS-E2.1G Model Output Prepared for CMIP6 CMIP* (Earth System Grid Federation, 2018).
70. NASA Goddard Institute for Space Studies (NASA/GISS). *NASA-GISS GISS-E2.1H Model Output Prepared for CMIP6 CMIP* (Earth System Grid Federation, 2018).
71. NASA Goddard Institute for Space Studies (NASA/GISS). *NASA-GISS GISS-E2.2H Model Output Prepared for CMIP6 CMIP* (Earth System Grid Federation, 2019).
72. Neubauer, D. et al. *HAMMOZ-Consortium MPI-ESM1.2-HAM Model Output Prepared for CMIP6 CMIP* (Earth System Grid Federation, 2019).
73. Yukimoto, S. et al. *MRI MRI-ESM2.0 Model Output Prepared for CMIP6 CMIP* (Earth System Grid Federation, 2019).
74. Thanwerdas, J. et al. Variational inverse modeling within the Community Inversion Framework v1.1 to assimilate $\delta^{13}C(CH_4)$ and CH_4: a case study with model LMDz-SACS. *Geosci. Model Dev.* **15**, 4831–4851 (2022).
75. Saunois, M. et al. The global methane budget 2000–2017. *Earth Syst. Sci. Data* **12**, 1561–1623 (2020).
76. Sindelarova, K. et al. High-resolution biogenic global emission inventory for the time period 2000–2019 for air quality modelling. *Earth Syst. Sci. Data* **14**, 251–270 (2022).
77. McDuffie, E. E. et al. A global anthropogenic emission inventory of atmospheric pollutants from sector- and fuel-specific sources (1970–2017): an application of the Community Emissions Data System (CEDS). *Earth Syst. Sci. Data* **12**, 3413–3442 (2020).
78. Crippa, M. et al. Gridded emissions of air pollutants for the period 1970–2012 within EDGAR v4.3.2. *Earth Syst. Sci. Data* **10**, 1987–2013 (2018).
79. Sindelarova, K. et al. Global data set of biogenic VOC emissions calculated by the MEGAN model over the last 30 years. *Atmos. Chem. Phys.* **14**, 9317–9341 (2014).
80. Wang, H., Liu, X., Wu, C. & Lin, G. Regional to global distributions, trends, and drivers of biogenic volatile organic compound emission from 2001 to 2020. *Atmos. Chem. Phys.* **24**, 3309–3328 (2024).
81. Andreae, M. O. Emission of trace gases and aerosols from biomass burning – an updated assessment. *Atmos. Chem. Phys.* **19**, 8523–8546 (2019).
82. Crippa, M. et al. *Fossil CO_2 and GHG Emissions of All World Countries* (Publication Office of the European Union, 2019).
83. Amann, M., Klimont, Z. & Wagner, F. Regional and global emissions of air pollutants: recent trends and future scenarios. *Annu. Rev. Environ. Resour.* **38**, 31–55 (2013).
84. van Marle, M. J. E. et al. Historic global biomass burning emissions for CMIP6 (BB4CMIP) based on merging satellite observations with proxies and fire models (1750–2015). *Geosci. Model Dev.* **10**, 3329–3357 (2017).
85. Huang, G. et al. Speciation of anthropogenic emissions of non-methane volatile organic compounds: a global gridded data set for 1970–2012. *Atmos. Chem. Phys.* **17**, 7683–7701 (2017).
86. Hoesly, R. M. et al. Historical (1750–2014) anthropogenic emissions of reactive gases and aerosols from the Community Emissions Data System (CEDS). *Geosci. Model Dev.* **11**, 369–408 (2018).
87. Zittel, W. & Altmann, M. Molecular hydrogen and water vapour emissions in a global hydrogen energy economy. In *Proc. 11th World Hydrogen Energy Conference* (1996).
88. Frazer-Nash. *Fugitive Hydrogen Emissions in a Future Hydrogen Economy* (Crown, 2022).
89. Xia, X., Zhou, H., Zhang, Y. & Jiang, H. Innovative steam methane reforming for coproducing CO-free hydrogen and syngas in proton conducting membrane reactor. *AIChE J.* **65**, e16740 (2019).
90. Barrett, M. & Cassarino, T. G. Heating with Steam Methane Reformed Hydrogen. Preprint at *Research Square* https://doi.org/10.21203/rs.3.rs-638496/v1 (2021).
91. USEPA. *Inventory of US Greenhouse Gas Emissions and Sinks: 1990-2015* Vol. 82, 10767 (USEPA, 2017).
92. Alvarez, R. A. et al. Assessment of methane emissions from the U.S. oil and gas supply chain. *Science* **361**, 186–188 (2018).
93. IEA. *The Future of Hydrogen: Seizing Today's Opportunities* (IEA, 2019).
94. Sitch, S. et al. Recent trends and drivers of regional sources and sinks of carbon dioxide. *Biogeosciences* **12**, 653–679 (2015).
95. Jickells, T. D. et al. A reevaluation of the magnitude and impacts of anthropogenic atmospheric nitrogen inputs on the ocean. *Global Biogeochem. Cycles* **31**, 289–305 (2017).
96. Paulsen, H., Ilyina, T., Six, K. D. & Stemmler, I. Incorporating a prognostic representation of marine nitrogen fixers into the global ocean biogeochemical model HAMOCC. *J. Adv. Model. Earth Syst.* **9**, 438–464 (2017).
97. Landolfi, A., Koeve, W., Dietze, H., Kähler, P. & Oschlies, A. A new perspective on environmental controls of marine nitrogen fixation. *Geophys. Res. Lett.* **42**, 4482–4489 (2015).
98. Wang, W.-L., Moore, J. K., Martiny, A. C. & Primeau, F. W. Convergent estimates of marine nitrogen fixation. *Nature* **566**, 205–211 (2019).

99. Warneck, P. *Chemistry of the Natural Atmosphere* (Elsevier, 1999).
100. Stoiber, R. E. in *Global Earth Physics: A Handbook of Physical Constants* (ed. Ahrens, T. J.) 308–319 (American Geophysical Union, 1995).
101. Canfield, D. E., Rosing, M. T. & Bjerrum, C. Early anaerobic metabolisms. *Philos. Trans. R. Soc. Lond. B Biol. Sci.* **361**, 1819–1834 (2006).
102. Constant, P., Poissant, L. & Villemur, R. Impact de la variation du niveau d'eau d'un marais du lac Saint-Pierre (Québec, Canada) sur les concentrations et les flux d'hydrogène, monoxyde de carbone, méthane et dioxyde de carbone. *Rev. Sci. Eau/J. Water Sci.* **18**, 521–539 (2005).
103. Khalil, M. A. K. et al. Emissions of methane, nitrous oxide, and other trace gases from rice fields in China. *J. Geophys. Res.* **103**, 25241–25250 (1998).
104. Conrad, R. & Babbel, M. Effect of dilution on methanogenesis, hydrogen turnover and interspecies hydrogen transfer in anoxic paddy soil. *FEMS Microbiol. Ecol.* **5**, 21–27 (1989).
105. Gilroyed, B. H., Chang, C., Chu, A. & Hao, X. Effect of temperature on anaerobic fermentative hydrogen gas production from feedlot cattle manure using mixed microflora. *Int. J. Hydrogen Energy* **33**, 4301–4308 (2008).
106. Saunois, M. et al. The Global Methane Budget 2000–2020. *Earth Syst. Sci. Data* **17**, 1873–1958 (2025).
107. Zimmerman, P. R., Greenberg, J. P., Wandiga, S. O. & Crutzen, P. J. Termites: a potentially large source of atmospheric methane, carbon dioxide, and molecular hydrogen. *Science* **218**, 563–565 (1982).
108. Tarmadi, D. Hydrogen and methane emissions by the lower termite *Coptotermes formosanus* Shiraki on various lignocellulose and lignin diets. *Jpn. J. Environ. Entomol. Zool.* **28**, 173–180 (2017).
109. Yanase, Y., Miura, M., Fujii, Y., Okumura, S. & Yoshimura, T. Evaluation of the concentrations of hydrogen and methane emitted by termite using a semiconductor gas sensor. *J. Wood Sci.* **59**, 243–248 (2013).
110. Pester, M. & Brune, A. Hydrogen is the central free intermediate during lignocellulose degradation by termite gut symbionts. *ISME J.* **1**, 551–565 (2007).
111. Sugimoto, A. et al. Methane and hydrogen production in a termite-symbiont system. *Ecol. Res.* **13**, 241–257 (1998).
112. Zellner, R., Wagner, G. & Himme, B. Hydrogen formation in the reaction of oxygen(1D) with water. *J. Phys. Chem.* **84**, 3196–3198 (1980).
113. Glinski, R. J. & Birks, J. W. Yields of molecular hydrogen in the elementary reactions hydroperoxo (HO_2) + HO_2 and atomic oxygen ($^1D_2$) + water. *J. Phys. Chem.* **89**, 3449–3453 (1985).
114. Hu, L. et al. Global budget of tropospheric ozone: evaluating recent model advances with satellite (OMI), aircraft (IAGOS), and ozonesonde observations. *Atmos. Environ.* **167**, 323–334 (2017).
115. Fu, T.-M. et al. Global budgets of atmospheric glyoxal and methylglyoxal, and implications for formation of secondary organic aerosols. *J. Geophys. Res.* **113**, D15303, (2008).
116. Myriokefalitakis, S. et al. The influence of natural and anthropogenic secondary sources on the glyoxal global distribution. *Atmos. Chem. Phys.* **8**, 4965–4981 (2008).
117. Silva, S. J., Heald, C. L. & Li, M. Space-based constraints on terrestrial glyoxal production. *J. Geophys. Res.* **123**, 13,583–13,594 (2018).
118. Bousquet, P. et al. A three-dimensional synthesis inversion of the molecular hydrogen cycle: sources and sinks budget and implications for the soil uptake. *J. Geophys. Res.* **116**, D01302 (2011).
119. Friedlingstein, P. et al. Global Carbon Budget 2021. *Earth Syst. Sci. Data* **14**, 1917–2005 (2022).
120. Sandoval, D., Prentice, I. C. & Nóbrega, R. L. B. Simple process-led algorithms for simulating habitats (SPLASH v.2.0): robust calculations of water and energy fluxes. *Geosci. Model Dev.* **17**, 4229–4309 (2024).
121. Ehhalt, D. & Rohrer, F. Deposition velocity of H_2: a new algorithm for its dependence on soil moisture and temperature. *Tellus B Chem. Phys. Meteorol.* **65**, 19904 (2013).
122. Ehhalt, D. H. & Rohrer, F. The dependence of soil H_2 uptake on temperature and moisture: a reanalysis of laboratory data. *Tellus B Chem. Phys. Meteorol.* **63**, 1040–1051 (2011).
123. Smith Downey, N. V. *Soil Uptake of Molecular Hydrogen and Remote Sensing of Soil Freeze and Thaw*. PhD thesis, California Institute of Technology (2007).
124. Bertagni, M. B., Paulot, F. & Porporato, A. Moisture fluctuations modulate abiotic and biotic limitations of H_2 soil uptake. *Global Biogeochem. Cycles* **35**, e2021GB006987 (2021).
125. Gasser, T. & Fu, B. tgasser/OSCAR: V3.3. *Zenodo*. https://doi.org/10.5281/ZENODO.10548477 (2024).
126. Alessandro, A. & Laura, B. D. *Hydrogen Emissions from a Hydrogen Economy and Their Potential Global Warming Impact: Summary Report of the Clean Hydrogen Joint Undertaking Expert Workshop on the Environmental Impacts of Hydrogen* (Publications Office of the European Union, 2022).
127. Esquivel-Elizondo, S. et al. Wide range in estimates of hydrogen emissions from infrastructure. *Front. Energy Res.* **11**, 1207208 (2023).
128. Fan, B. Y. Z. et al. *Hydrogen Leakage: A Potential Risk for the Hydrogen Economy* (Center on Global Energy Policy, 2022).
129. Solazzo, E. et al. Uncertainties in the Emissions Database for Global Atmospheric Research (EDGAR) emission inventory of greenhouse gases. *Atmos. Chem. Phys.* **21**, 5655–5683 (2021).

Acknowledgements This work is part of an international effort coordinated by the Global Carbon Project. We thank M.O. Andreae for calculating the GFAS-burnt biomass data for the period 2008–2017 (not used in the study), based on data provided by J. Kaiser and I. Hüser; J. Kaiser for helping update H_2 and VOC emissions from GFAS-burnt biomass based on updated emission factors; S. Sitch for helping us access TRENDY authors and data; B. Zheng for his suggestions on using CO emission data; D.A. Tran for the help in gap-filling early H_2 mixing ratio data; R.G. Derwent for assistance with H_2 data from the AGAGE network; S. Smith for his advice on using the CEDS emission data; K. Sindelarova for help with biogenic VOC emission products; W. Winiwarter for sharing the ECLIPSE v.6b data; A.S. Darmenov for providing us support and instructions on how to use QFED; L. Emmons and C. Wiedinmyer for help using the FINN fire emission dataset; P. Anthoni for help on LPJ-GUESS BNF data; J. Patterson for sharing H_2 concentration data reconstructed from firn air; and X. Yu for helping some data conversions, and S. Karbin for useful insights in soil H_2 uptake modelling. D.H. thanks M. Beaudor for her help with the ORCHIDEE model dataset. R.B.J. acknowledges support from the Stanford Doerr School of Sustainability, GCP Global Methane Office of Stanford, and the Gordon and Betty Moore Foundation, grant GBMF11519. Z.O. acknowledges support from the Stanford Doerr School of Sustainability, and the College of Forestry, Wildlife and Environment at Auburn University, and the Gulf Research Program of the National Academies of Sciences, Engineering, and Medicine (SCON-10001693). E.K. was supported by the ERTDF (JPMEERF24S12206) of the ERCA by the Ministry of the Environment of Japan. G.P. was supported by NOAA cooperative agreements NA17OAR4320101 and NA22OAR4320151. G.P.P. was supported by the Research Council of Norway project TRIFECTA (334811). A.T.A. was supported by the Natural Environment Research Council (NERC NE/X010236/1). M.W.J. was supported by the Natural Environment Research Council (NERC, NE/V01417X/1). F.G. was supported by DOE DE-SC0020480 and thanks J. Roscioli, E. Lunny and J. Shorter for guiding the experimental setup. C.W. was supported by the US Department of Energy (DOE) National Energy Technology Laboratory under grant no. DE-FE0032285. T.G. and D.H. were supported by the Horizon Europe research and innovation programme of the European Union under grant agreement no. 101137582 (HYway). C.M. was supported by the LEMONTREE (Land Ecosystem Models Based on New Theory, Observations and Experiments) project, supported by Schmidt Sciences. N.C. and P.K.P. are funded by the ERTDF (JPMEERF24S12205) of the ERCA by the Ministry of the Environment of Japan. P. Smith acknowledges funding from UK NERC grant no. NE/X013464/1. C.D.J. was supported by the Met Office Hadley Centre Climate Programme funded by DSIT.

Author contributions Z.O., R.B.J. and J.G.C. designed, conceptualized and coordinated the study. R.B.J. secured funds for this study. Z.O. wrote the original draft. Z.O., R.B.J., J.G.C., M.S., Y.Z., C.M., P.B.K., P.K.P., G.P.P., F.D. and T.K. prepared the main datasets, conducted the main data analysis and synthesis, and wrote the paper. M.S. provided methane emission data and 3D CH_4 concentration data. Y.Z. conducted an estimation of H_2 production from CH_4 oxidation and H_2 loss through reacting with OH. C.M. provided the model for estimating soil H_2 uptake and helped implement the model. P.B.K. prepared and processed the atmospheric observations of H_2. G.P.P. helped with the future H_2 economy scenarios and climate response estimates. T.G. estimated the climate impact of H_2 and G.B. helped implement the relevant models. P.K.P. provided 3D CH_4 concentration data. F.D. prepared the OH field data. A.T.A. updated information on the yield of HCHO from different NMVOCs. P.C., P. Smith, S.J.D., C.D.J., M.W.J., B.P., J.R. and H.T. commented on, edited or discussed the early version of the paper through to its final iteration. D.H. provided ORCHIDEE simulation and OH fields. P. Suntharalingam provided NEMO-PlankTOM model simulation of biological nitrogen fixation. V.A. and J.R.M. provided CLASSIC simulation. E.K. provided VISIT simulation. D.K. and D.L. provided different versions of CLM5.0 simulation. J.K. provided CABLE-POP simulation. S.L. provided LPX-Bern simulation. J.E.M.S.N. provided JSBACH simulation. M.O. and A.W. provided different versions of JULES simulation. D.S.C. provided SPLASH simulation. G.P. helped accessing and using NOAA H_2 observation data. S.F. helped with processing H_2 observational data. C.W. helped with processing fire emission data. N.C. implemented the 2D box model for budget evaluation. F.G. contributed new measurements of H_2 emissions from legume plants. All co-authors reviewed and edited the paper.

Competing interests The authors declare no competing interests.

Additional information

Supplementary information The online version contains supplementary material available at https://doi.org/10.1038/s41586-025-09806-1.

Correspondence and requests for materials should be addressed to Robert B. Jackson.

Peer review information *Nature* thanks the anonymous reviewers for their contribution to the peer review of this work. Peer reviewer reports are available.

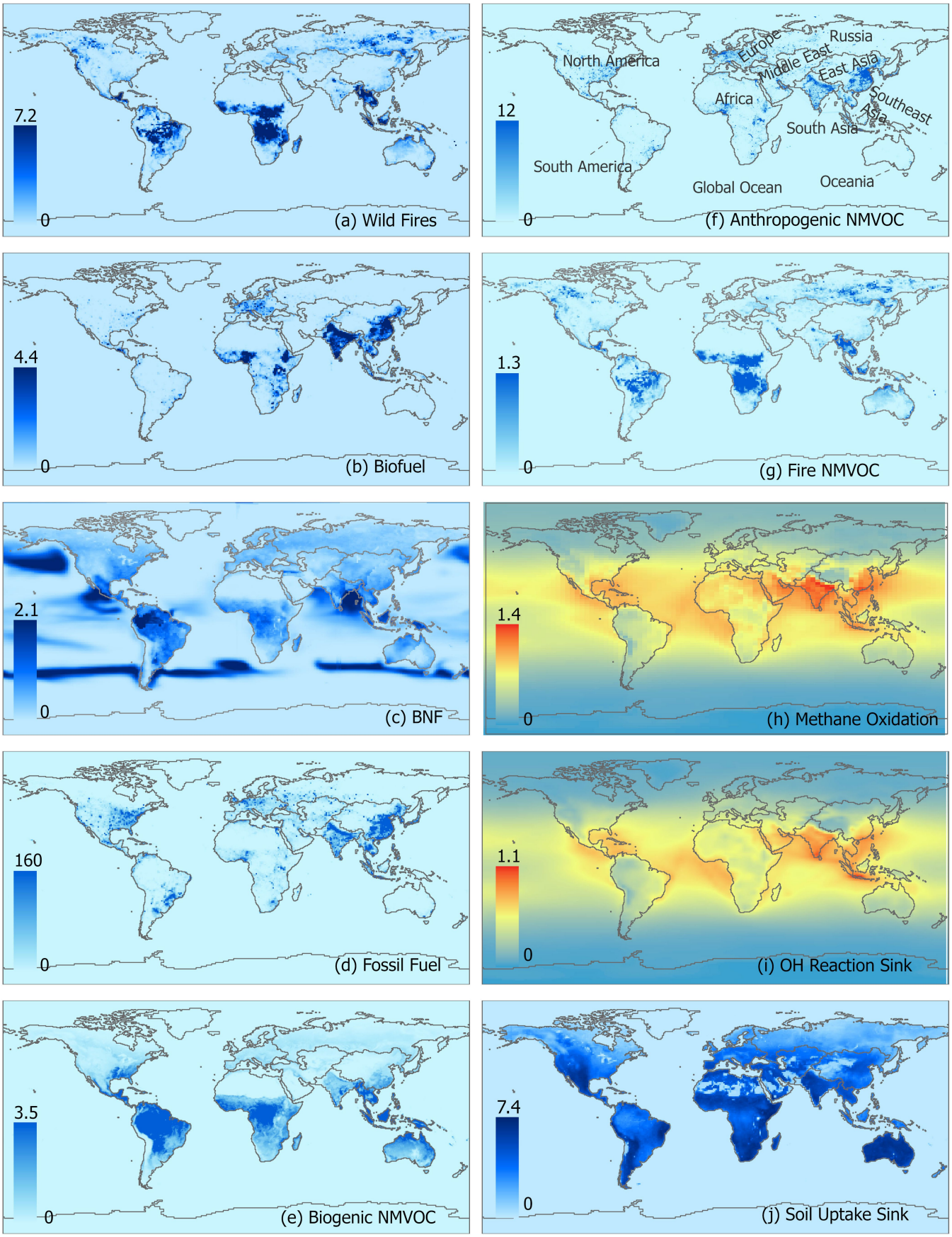

Extended Data Fig. 1 | The spatial distribution of H_2 sinks and sources. These include direct emission from wildfires (a), Biofuel (b), Biogenic Nitrogen Fixation (BNF) (c), fossil Fuel usage (d), and production from oxidation of biogenic non-methane volatile organic compounds (NMVOC) (e), anthropogenic NMVOC (f), fire emitted NMVOC (g), and methane (h), and sinks of OH reaction (i) and soil uptake (j).

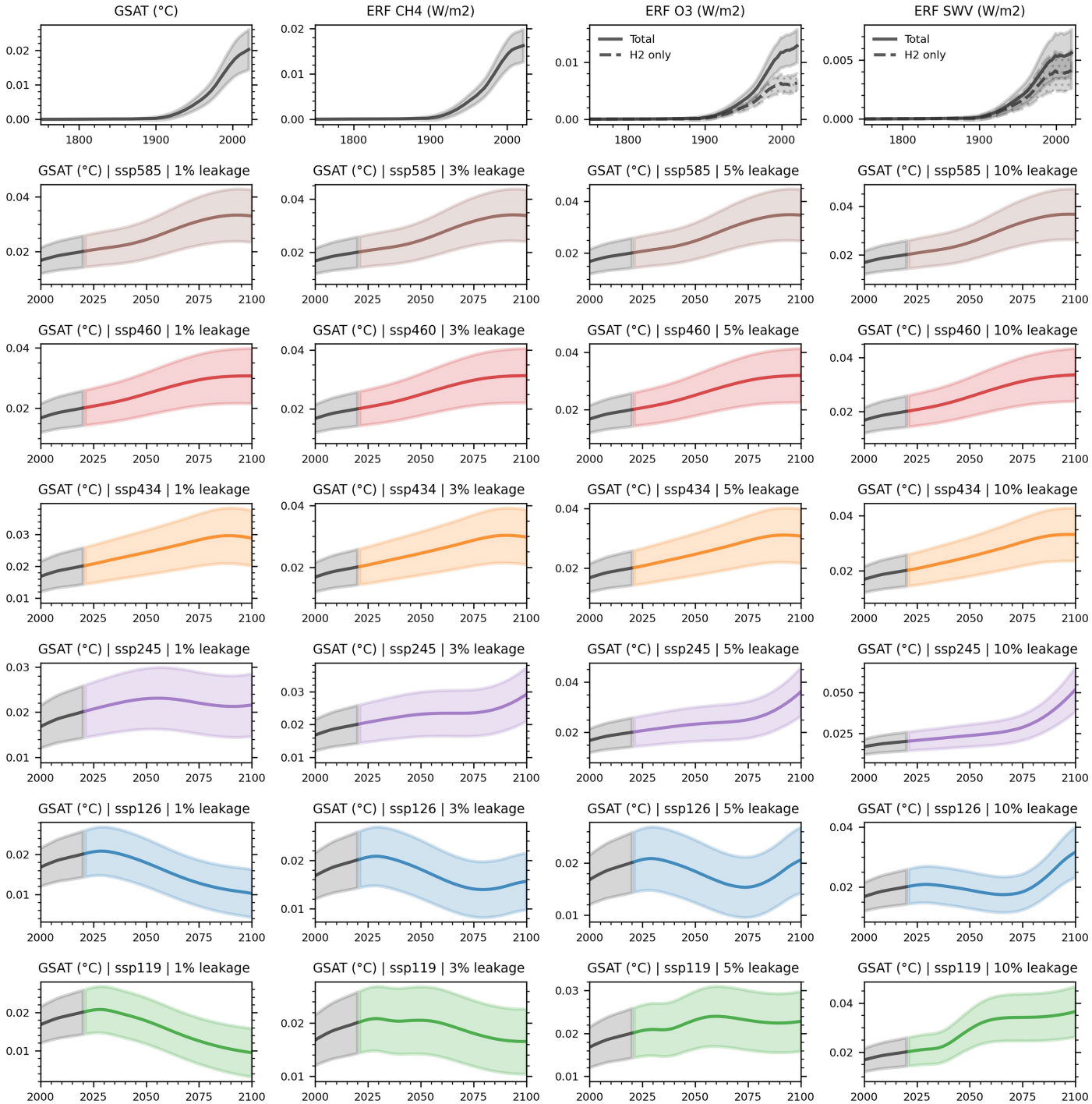

Extended Data Fig. 2 | Historical and projected global surface air temperature (GSAT) changes caused by having H_2 represented in the model at different economy-wide H_2 leakage rates. This is obtained as the difference between a fully interactive simulation and a counter-factual one in which H_2 concentration is kept at preindustrial level. Top-row panels show the historical contribution of H_2 to GSAT, as well as to CH_4, O_3 and stratospheric water vapor (SWV) effective radiative forcings (ERF). All other panels show projected contribution to GSAT, under difference marker SSPs and leakage rates, as indicated in the panels' titles.

Extended Data Table 1 | Mean global sinks and sources (Tg H_2 yr^{-1}) averaged for the period 2010–2020

Period	2010-2020	2020
Sources		
Fossil fuel	**7.5±3.9** (10.7%)	**6.8±3.8** (9.8%)
Automobile Transportation	3.7±2.0	2.9±1.8
Other processes	3.8±3.3	3.9±3.4
Biomass burning	**11.6±3.7** (16.6%)	**11.9±4.2** (17.3%)
Open fires	8.4±3.3	8.9±3.9
Biofuels	3.2±1.7	3.0±1.5
Biogenic N_2 fixation	**8.0±4.0** (11.6%)	**7.8±3.9** (11.3%)
Ocean	4.9±3.1	4.6±2.9
Land	3.1±2.5	3.2±2.6
Photochemical production	**38.4±6.1** (54.9%)	**37.7±6.0** (54.7%)
CH_4 Oxidation	26.1±3.5	25.3±3.3
NMVOC Oxidation	12.3±5.0	12.4±5.0
biogenic NMVOCs	*10.7±5.0*	10.8±5.0
Wildfire NMVOCs	*0.5±0.3*	*0.5±0.3*
Anthropogenic NMVOCs	*1.1±0.6*	*1.1±0.6*
Leakage from H_2 production	**0.7±0.4** (1.0%)	**0.9±0.5** (1.3%)
Other minor sources	**3.7±2.3** (5.2%)	**3.8±2.3** (5.6%)
Sinks		
Soil uptake	**50.0±18.0** (73.0%)	**51.1±18.4** (73.6%)
OH reaction	**18.4 ±2.2** (27.0%)	**18.3 ±2.2** (26.4%)
Net Imbalance		
Bottom up	**1.5±20.4**	**-0.5±20.8**
Optimized	**0.6±1.4**	**1.1**
H_2 Lifetime		
2.8 Year		

The percentage relative to the total estimated sources or sinks is displayed in parentheses. The Optimized net imbalance was obtained using a two-box model to agree with observed atmospheric H_2 concentrations as described in Supplementary Note 2.

Extended Data Table 2 | Summary of available empirical data and critical needs on H_2 emissions and uptake

Category	Data Availability Level and Description	Critical Needs
Soil H_2 Uptake Rates	**Some**: A few sites with season-long measurements	More long-term, year-round measurements across diverse ecosystems, climate zones, and soil types.
Soil Maximum Biological Oxidation Rate	**Rare**: Only a single measured value reported in literature	Laboratory-based studies needed to determine maximum biological oxidation rates for soils with varying textures and properties.
Leakage Rates of H_2 from Facilities	**Rare**: No empirically measured leakage data available in the literature for production sites, pipelines, end-use infrastructure, or appliances.	Development of new instrumentation for detection; systematic field measurements across a range of facility types and infrastructure components.
Biomass Combustion	**Some**: Emission factors are available for certain wildfire types and biofuel appliances based on one or just a few measurements	Broader measurement campaigns needed to capture variability and uncertainty across combustion types and regions.
Fossil Fuel Combustion	**Some**: Existing measurements were mainly focused on older generation vehicular emissions in Europe.	Expanded data collection across different vehicle types, fuel compositions, regions, and other fossil fuel applications beyond transportation.
Biogenic Nitrogen Fixation-Land	**Rare**: One study includes full season-based measurements	More long-term measurements of various legume species, with coordinated monitoring of both nitrogen fixation rates and associated H_2 emissions.
Biogenic Nitrogen Fixation-Ocean	**Some**: Limited field and laboratory studies provide short-term ratios of H_2 emissions to N fixation.	Increased spatial and temporal coverage is needed, including long-term observations in under-sampled marine regions.
VOC Oxidation	**Some**: A few studies provide yield estimates of formaldehyde (HCHO) production from different VOC groups.	New measurements and experimental studies required to refine HCHO yield rates under different atmospheric conditions for various VOC groups.
Other minor sources	**Some:** Scattered emission factors exist for various sources including geological seepage, wetlands, rice paddies, landfills, wastewater treatment, termites, and livestock.	Additional targeted measurements are needed, especially for geological sources and termites, which may contribute more significantly than currently estimated.

Two levels of data availability are defined here: Some—limited measurements from a few studies, and Rare—nearly none or only one related study provides data.